Oil & Natural Gas Technology

Structural and Stratigraphic Controls on Methane Hydrate occurrence and distribution: Gulf of Mexico, Walker Ridge 313 and Green Canyon 955

Final Technical Report

Report Period: 10/01/2012 – 07/31/2016

Principal Author: Priyank Jaiswal

Date of issue: 01/09/2017

DOE Award No.: DE-FE0009904

Boone Pickens School of Geology, Oklahoma State University

DUNS # 049987720.

Stillwater, Oklahoma 74075

Office of Fossil Energy

Disclaimer

This report was prepared as an account of work sponsored by an agency of the United States Government. Neither the United States Government nor any agency thereof, nor any of their employees, makes any warranty, express or implied, or assumes any legal liability or responsibility for the accuracy, completeness, or usefulness of any information, apparatus, product, or process disclosed, or represents that its use would not infringe privately owned rights. Reference herein to any specific commercial product, process, or service by trade name, trademark, manufacturer, or otherwise does not necessarily constitute or imply its endorsement, recommendation, or favoring by the United States Government or any agency thereof. The views and opinions of authors expressed herein do not necessarily state or reflect those of the United States Government or any agency thereof.

Executive Summary

The goal of this project was to determine structural and stratigraphic controls on hydrate occurrence and distribution in Green Canyon (GC) 955 and Walker Ridge (WR) 313 blocks using seismic and well data. Gas hydrate was discovered in these blocks in coarse- and fine-grained sediments during the 2009 Joint Industrial project (JIP) Leg 11 drilling expedition. Although the immediate interest of the exploration community is exclusively hydrate which is present in coarse–grained sediments, factors that control hydrate and free gas distribution in the two blocks and whether coarse and fine-grained hydrate-bearing units are related in any manner, formed the core of this research.

The project spanned from 10/01/2012 to 07/31/2016. In the project, in both the leased blocks, the interval spanning the gas hydrate stability zone (GHSZ) was characterized using a joint analysis of sparse Ocean Bottom Seismic (OBS) and dense, surface–towed multichannel seismic (MCS) data. The project team had the luxury of calibrating their results with two well logs. Advance processing methods such as depth migration and full-waveform inversion (FWI) were used for seismic data analysis. Hydrate quantification was achieved through interpretation of the FWI velocity field using appropriate rock physics models at both blocks.

The seismic modeling/inversion methodology (common to both GC955 and WR313 blocks) was as follows. First, the MCS data were depth migrated using a P-wave velocity (V_P) model constructed using inversion of reflection arrival times of a few (four in both cases) key horizons carefully picked in the OBS data to farthest possible offsets. Then, the resolution of the traveltime V_P model was improved to wavelength scale by inverting OBS gathers up to the highest frequency possible (21.75 Hz for GC955 and 17.5 for WR313) using FWI. Finally, the hydrate saturation (or the volume fraction) was estimated at the well location assuming one of the other hydrate morphology (filling the primary or the secondary porosity) was extrapolated out from the wells using the FWI V_P as a guide.

General outcomes were as follows. First and foremost, an imaging methodology using sparse seismic data, which is easily replicable at other sites with similar datasets, has been demonstrated. The end product of this methodology at both the leased blocks is quantitative estimates of hydrate distribution. Second, at both locations there is strong evidence that the base of the GHSZ, which does not appear as a clear Bottom Simulating Reflection (BSR), manifests in the V_P perturbations created by FWI, suggesting that FWI is sensitive to subtle compositional changes in shallow sediments and establishes it as a valuable tool for investigations of hydrate-bearing basins. Third, through joint interpretation of the depth migrated image and the FWI V_P model, how structure and stratigraphy jointly determine hydrate and free gas distribution in both blocks could be clearly visualized. The joint interpretation also suggests that the coarse and fine grained hydrate-bearing sediments at both leased are connected.

Site specific results, in addition to general results, are as follows. At GC955 the overlying fine-grained hydrate-bearing unit could have been sourced from the underlying hydrate coarse-grained channel-levee complex through a chimney feature. The channel-levee system at GC955 is compartmentalized by faults, of which only a few may be impermeable. Although compartmentalized, the channel-levee system in the GC955 as a whole might be in communication except selected zones. At WR313 the overlying fine-grained fracture-filled hydrate unit appears to be sourced from below the GHSZ. The reason that only a particular fine-grained unit has hydrate, despite having lower porosity that the bounding units, could be the presence of secondary porosity (such as those formed from clay dewatering under compaction).
In conclusion, the project was a pioneering effort in in joint analysis of OBS and MCS datasets for advancing the knowledge about a hydrate and free–gas system dynamics using advanced processing methods such as FWI and depth migration.

Results obtained in this project can greatly advance the tools and techniques used for delineating specific hydrate prospects. Results obtained in this project can also be seamlessly incorporated into other DOE

funded project on modeling the potential productivity and commercial viability of hydrate from sand-dominated reservoirs. The OBS and MCS data in this project were acquired in 2012 (after the JIP II drilling) by the USGS and therefore the results are *a posteriori*. Nonetheless, the seismic inversion workflow established through this project can be used to generate various what-if quantification scenarios even in absence of logs and serve as a valuable tool for guiding drilling operations. Results from this project can augment other DOE sponsored projects on determining the commercial viability of methane production from the Gulf of Mexico.

Table of Contents

Background

Gas hydrates are ice-like substances composed of water and gas that precipitate from light hydrocarbon-charged water at moderately high pressure, low temperature, and low salinity. Enormous quantities of hydrate and associated free gas occur beneath the seafloor along continental margins (Milkov 2004). Hydrocarbons in these phases, principally CH_4, may constitute a future energy resource (Boswell and Collett 2011), a deep-water geohazard (McConnell et al. 2012b), and a large component of the carbon cycle (Dickens 2001), which could impact the environment if perturbed (Kvenvolden 1999). In theory, gas hydrates can form in marine sediment wherever light hydrocarbons saturate pore waters between the seafloor and the base of gas hydrate stability (BGHS) (Sloan 1998). The global hydrate stability zone (HSZ), which in places can be as deep as a 1000 m below seafloor (mbsf), is expensive and impractical to investigate through drilling. Instead, the amount and distribution of hydrate in ocean sediments is largely understood through limited seafloor observations, scientific boreholes in selected locations, numerical models, and geophysical imaging.

These geophysical and subsurface investigations have so far indicated that gas hydrates are heterogeneously distributed at multiple scales. They also indicate that gas hydrates exhibit a variety of arrangement styles such as filling pore space (Nankai Prism; Kida *et al.*, 2009), being embedded in rock matrix (Mackenzie Delta; Winters *et al.*, 2004), and cementing within (or) around mineral grains (Oseberg Field; Dvorkin and Nur, 1996). In fine-grained sediments, they create and occupy fractures (Gulf of Mexico; Hutchinson *et al.*, 2008) and form massive nodules (Hydrate Ridge; Bohrmann *et al.*, 1998). This heterogeneity and multiple arrangement styles have been documented in Ocean Drilling Program (ODP) cores from the Blake Ridge (Leg 164) (Paull et al. 1996) and Hydrate Ridge (Leg 204) (Tréhu et al. 2003) and the National Gas Hydrate Program (NGHP-01) cores from the Krishna Godavari Basin (Collett et al. 2007). Observations of these cores clearly show that hydrate abundance varies at cm- to m-scale down boreholes, probably because of differences in lithology and pore size (Weinberger et al. 2005).

The northern Gulf of Mexico (GoM) has been a focus area for hydrate research since physical sampling of gas hydrate at the Bush Hill site in 1980s (Brooks et al. 1986). Even though the variable salinity and temperature in the GoM deters formation of classic diffusive-margin-type bottom simulating reflector (BSR) (McConnell and Kendall 2003), multiple reports of hydrate outcropping at the ocean floor (McDonnell et al. 2000) has kept the search for "buried" hydrate alive (Hutchinson et al. 2011). Search for hydrate in the GoM has strategic implications for the United State (US). Not only discovery of hydrate in economically viable production quantities can improve the energy security of the country, a detailed on hydrate growth and formation can also ensure platform safety (Sassoon 2010). From a "petroleum systems" perspective, the GoM has favorable elements that create a prolific hydrate basin, such as high gas charge (both thermogenic and biogenic) and reservoir quality sand bodies. Hydrate exploration driven by a "petroleum system" philosophy was first tested in 2005 through a collaborative effort between government and GoM operators (the Joint Industry Project; JIP). Presence of buried gas hydrates was confirmed in the 1st Leg of JIP (Ruppel et al. 2008). During this period, the Bureau of Ocean Energy Management (BOEM) was also conducting assessment of the GoM hydrate petroleum systems (Frye 2008), suggesting presence of over 21 TCF gas-in-place, with roughly one-third of that in high concentrations found in sand reservoirs. BOEM also documented 145 geophysical signatures potentially representing the BHSZ (Shedd et al. 2012).

The most ambitious and successful hydrate expedition was carried out in the GoM in 2009 in the 2nd Leg of the JIP where seven holes spanning across lease blocks Walker Ridge (WR) 313, Green Canyon (GC) 955, and Atwater Canyon (AC) 21, were drilled and logged using a comprehensive set of logging-while-drilling (LWD) tools (Collett et al. 2012a). JIP Leg 2 was successful in hydrate detection in highly concentrated forms (>60% saturation) within the sand-dominated reservoirs (Boswell et al. 2012a). With near-future technology, the recovery of these hydrates is highly possible. This report characterizes hydrate bearing sediments at GC955 and WR313.

Summary of the JIP Leg 2 findings at GC955 and WR313

GC955

In GC955 the target was a Pleistocene channel-levee complex (Collett et al. 2012b). Three drilling locations were determined in GC955 using existing industry seismic and well data (Hutchinson et al. 2008a). The first well, GC955-I, at water depths of 2063.5 m, encountered the channel-levee complex with 362-479 mbsf depth interval (Collett et al. 2012b). However, within over 100m of the target zone, less than one meter of sediments was inferred to be hydrate rich (Boswell et al. 2012b). The second well, GC955-H, 1.5 km southwest of Well I, was placed in water depth of 2024 m and penetrated two types of hydrate reservoirs – a fine-grained fractured unit within 192-308 mbsf depth interval and a 20m thick sandy unit within the target channel-levee section which spanned from 413 mbsf to 450 mbsf (Collett et al. 2012b). Using the ring resistivity and sonic logs Lee and Collett (2012a) estimated hydrate saturations to be ~20% in the fine-grained strata and at least 60% in the sandy unit. The third well, GC966-Q, was located 1.5km southwest of Well H in water depths of 1978 m and encountered the channel-levee complex at 429 mbsf. However, after only drilling through 9m, drilling had to be abandoned as free gas was suspected below the borehole (Boswell et al. 2012b).

The most intriguing aspects of the GC955 drilling campaign was the dramatic difference in the thickness of hydrate-bearing sediments between Wells H and Q despite being only ~1.5 km apart and seemingly forming part of a common channel-levee feature (Boswell et al. 2012b). At well H three hydrate-rich sandy units have been interpreted –26.8 m thick upper unit, 1m thick middle unit and 0.6m thick lower unit. In Well Q, the thickness of the hydrate-bearing sandy layer is probably only 9m. Additionally, the fine-grained fractured unit in which Well H encountered gas hydrate continues up to Well Q, but no evidence of hydrate was found at that location.

WR313

At WR313 two sites, G and H, were occupied. The site lies within the Terrebonne mini-basin, which is north-south elongated basin bounded by a salt-core ridge that divides the basin into separate eastern and western sub-basins (McConnell et al., 2010; Boswell et al., 2012a). Both the JIP Leg II sites were located on the eastern margin of the western part. Pre-drill interpretation of an east-west profile connecting the two sites showed that the general stratigraphy is dipping ~8-12° east (Boswell et al., 2012a). Further, three units, referred to as "blue," "orange" and "green," in increasing order of age and depth, were considered of interest because it appeared from seismic inversion that they could dominantly comprise coarse grained sediments (McConnell et al., 2010). Inversion results also suggested that the blue and orange units may have high gas hydrate saturations. The drilling was meant to primarily log these three units and also to test the interpretation that intermittent phase reversals can be used as a reliable proxy of the gas hydrate stability zone (GHSZ).

The drilling results were encouraging in that elevated resistivity and sonic were observed within "blue" and "orange" units. The general log character strongly suggested that a) these units are coarse grained and b) they contain hydrate. A high resistivity zone shallower than the blue unit was also encountered at both sites and was interpreted as a clay-dominated unit with hydrate-filled fractures (Collett et al., 2012; Cook et al., 2012). At site G drilled in 2000m water depth, the shallow zone of elevated resistivity was between 237 mbsf and 402 mbsf. The “blue” unit was encountered at 774 mbsf. From logs it was inferred that this unit comprised 21 m gross interval of interbedded sand and mud with ~9 m net coarse grained sediments containing high hydrate saturation. The “orange” unit at site G was below the interpreted GHSZ. It was inferred as a clay-rich interval with minor water-bearing sands. The “green” unit was deeper than the total drilling depth at site G.

WR311-H was drilled ~1.85 km east up-dip of Site G in a water depth of 1966m. Similar to site G, the fracture-filling hydrate zone was found between 168-314 mbsf (Collett et al., 2012). The “blue” unit was encountered at the depth of ~649mbsf. Compare to the G site, the hydrate saturated part of this unit was significantly thinner and more mud-proned (McConnel et al., 2010). The “orange” unit was encountered at 806 mbsf and out of 13m gross thickness, only 8.2 m was interpreted as gas hydrate-bearing sand (Frye et al., 2012). The “green” unit was ~75m below the interpreted GHSZ and the unit was inferred to be fully water saturated (Boswell et al., 2012b). In summary, none of the three unit was found to be hydrate-bearing massive sand. Further, only the “blue” units was within the GHSZ at both sites and appeared to be having highly variable sand and hydrate content.

The JIP Leg 2 drilling results were intriguing. While bodies of hydrate-bearing sands exist at all sites, they are laterally and vertically juxtaposed against clay-dominated, fractured sediments. Close proximity of the two hydrate reservoirs with vastly different mineralogy, grain-size, and porosity, has given rise to several significant questions related to the long term behavior of hydrate growth and dissociation in presence of natural or artificially induced fluid flow. The main knowledge gap that emerged out of JIP Leg 2 drilling sites that were addressed in this project include:

a. *Heterogeneity of hydrate distribution within sand reservoirs*: Sand-dominated reservoirs are currently viewed as a single continuous mass of sediment, where hydrates are homogenously distributed within pores (Lee and Collett 2012b). Our results show that this assumption may not be strictly true. In general, the sand-rich channel deposits in the GoM have been found to demonstrate large variations in sediment size and porosity (Prather 2003, Weimer 1990). As a result, detailed imaging and characterization of sand-dominated reservoirs at all sites visited in JIP Leg 2 is needed. Addressing this aspect is a key to future developments of hydrate-bearing sand bodies as potential reservoirs.

b. *Association of fracture-dominated and sand-dominated reservoirs*: Currently for characterization purposes, the fine-grained, fracture-dominated and the coarse-grained sand-dominated reservoirs are being treated as separate entities (Zhang et al. 2012). Although seismic images clearly show that both reservoir types are penetrated by common fault, there is a lack of information on whether hydrate in the sand-reservoir serve as source or sink for hydrate-filled fractures, or whether the two systems are completely unrelated. Furthermore, there is a lack of interpretation to determine if fractures in the clay-dominated sediments are stand-alone or if they are working as relay-system. Addressing this may hold the key to understanding free gas migration from below the BHSZ up to the seafloor followed by its potential release into the overlying ocean.

For overall characterization of the hydrate bearing sediments logged in JIP Leg II, US Department of Energy (DOE), US Bureau of Ocean Management (BOEM) and the United States Geological Survey (USGS) acquired coincident OBS and high-resolution MCS data (Haines et al., 2014). These data were acquired using two 105/105 cu. in. generator-injector airguns which provided a source wavelet with a frequency range of 50-250 Hz. The project team used these data to create a high-resolution reflectivity image as well as a velocity model along selected profiles at GC955 and WR313 and quantitatively interpreted them using rock physics models. This effort finally resulted in quantitative prediction of hydrate content in the host sediments at both sites and addressed the knowledge gaps highlighted above.

In this report, processing of two profiles are being presented – one from GC955 and the other from WR313. In GC955, a profile connecting Wells H and Q was processed. This profile had 10 collocated OBSs (Figure 1b). In WR313, a profile connecting Wells H and G was processed. This profile had 9 collocated OBSs (Figure 1c). The processing approach for both transects is almost identical except the rock physics modeling. The processing was completed in three phases. In the first phase, a large-sale (resolution in the order of Fresnel zone) P-wave velocity (V_P) model was created using traveltime inversion along with its corresponding depth image using depth migration of the MCS data. In the second phase, the resolution of the P-wave velocity model created in the first phase was refined to the order of seismic wavelength using full-waveform inversion (FWI) of the OBS data. In the third phase, a hydrate distribution map was created by rock physics interpretation of the V_P model from the second phase. In GC955, a rock physics model appropriate for coarse grained sediment was chosen and in WR313, a model appropriate for fractured sediments is chosen. This is because of the limited resolution of the seismic data. At both sites GC955 and WR313, although hydrate was present in coarse and fine grained sediments, only the coarse grained target at GC955 and fine grained at WR313 could be seismically resolved. Finally, the FWI V_P models, the hydrate saturation maps and the PSDM image were jointly interpreted to address the main knowledge gaps highlighted above.

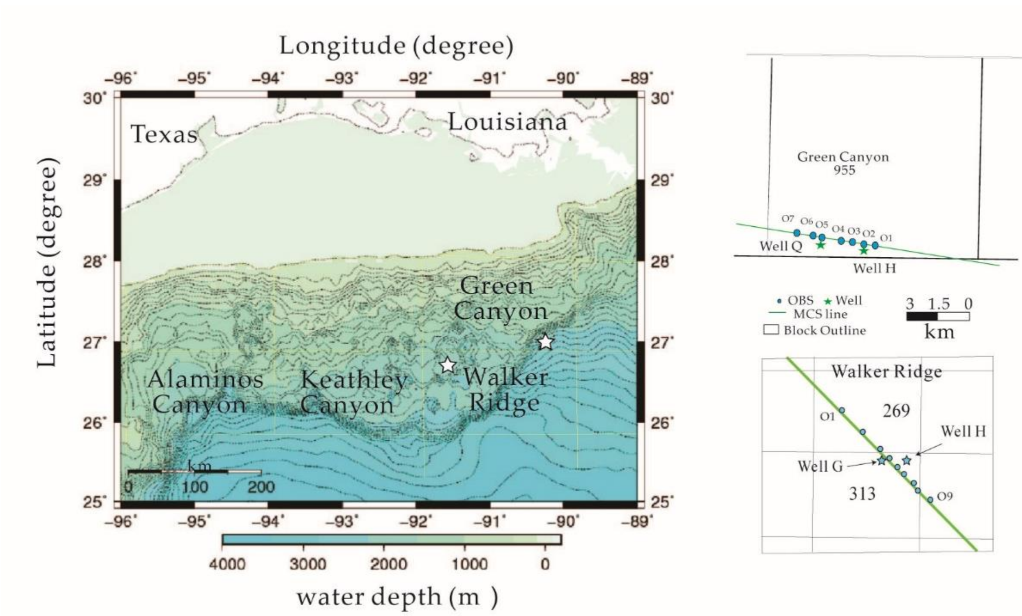

Figure 1. Base map. Location of the study area in the Gulf of Mexico. Location of the seismic line, wells and OBSs with respect to the block boundaries are shown in independent sketches.

Approach

For both datasets, WR313 and GC955, the overall processing approach was as follows. First, the OBS data were decomposed to separate the up- and downgoing parts. The downgoing part, which is essentially the bubble pulse was discarded. Only the upcoming part, which is essentially the reflection, was used for processing. The upcoming wavefield, hereafter generally referred to as "OBS gather", was merged with MCS stack to identify commons reflections. These reflection times were used for traveltime inversion. Using the traveltime inversion solution as the starting mode, the OBS gathers were inverted using a frequency-domain full waveform inversion (FWI) code. Prior to inversion the OBS gathers were scaled and therefore FWI was only used to extract velocity information and not attenuation. Finally the FWI velocity model was compared to the sonic logs at both GC955 and WR313 sites to select an appropriate model for hydrate quantification. Sections 2.1 – 2.6 are common to datasets from both sites.

Wavefield Decomposition

Seismic events in OBS data comprise direct waves, primary reflections, source-side ghost, water-column reverberations, free-surface multiples and internal multiples. The recorded wavefield in OBS data can be divided into up- and downgoing parts according to the wave arrival directions. The downgoing wavefield contains the direct wave, receiver-side multiples and water-column reverberations, while the upgoing wavefield includes all the primaries and source-side ghosts and internal multiples. Since the primary reflections are the main parts in our traveltime modeling, the upgoing wavefield is employed to attenuate the water-column reverberation and receiver-side multiples. Combination of the pressure and the vertical geophone (velocity) components results in the up- and downgoing wavefield. This is because pressure is a scalar quantity and up- and downgoing pressure wavefield gets the same polarity on hydrophone recordings while the up- and downgoing pressure wavefield show opposite polarities on vertical geophone recording. Therefore, upgoing and downgoing wavefield can be separated as:

$$\begin{aligned} U &= (P + \alpha Z)/2 \\ D &= (P - \alpha Z)/2 \end{aligned} \tag{1}$$

where U is the upgoing wavefield, D is the downgoing wavefield, P is pressure as recorded on the hydrophone, Z is particle velocity recorded on the vertical geophone, α is a scalar (Grion et al., 2007). The wavefield decompositions attenuates multiples and source reverberations but not bubble effects and swell noise (Figure 2). Nonetheless the overall data quality was better after wavefield decomposition. Predictive deconvolution and bandpass filter were also applied to the upgoing OBS wavefield to further improve data quality.

MCS data and processing

The MCS data were acquired using 72 channel, 450 m long hydrophone steamer cable with 6.125 m receiver spacing and 40m near-offset and 1-ms sampling interval. The shot interval was approximately 25 m. The GC955 transect contains 280 shots and the WR313 303 shots. Overall, the MCS data had high signal-to-noise ratio and was processed only minimally. At both sites, the processing flow included spherical divergence correction followed by 10-200 Hz band-pass filter, normal move-out (NMO) correction and stacking. The stacking velocity profile was a simple gradient – 1480 m/s at the seafloor linearly increasing to 2500 m/s 2.5s below the seafloor. The intent of MCS processing was only to generate a stack to identify key horizons and stratigraphic features within the hydrate stability zone.

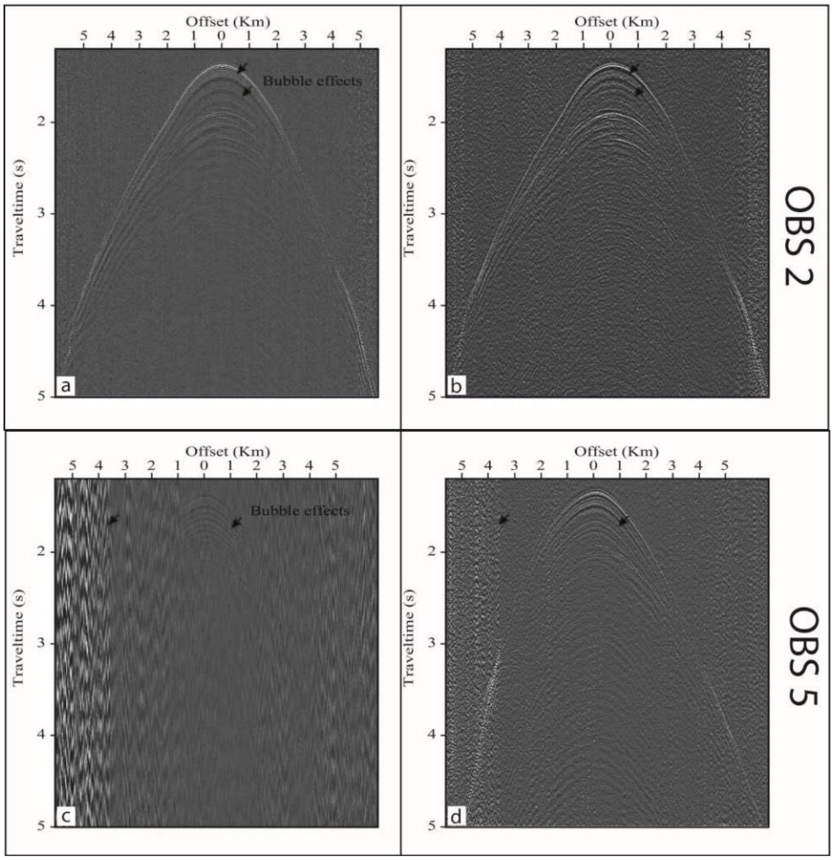

Figure 2. Wavefield separation at GC955. The left columns show the upgoing wavefield after decomposition. The right columns display the data after predictive deconvolution and bandpass filter. These data after denoising are used to pick traveltimes for inversion.

Locating OBSs along the MCS profile

At both site, the profiles have a number of collocated OBSs. One of the key challenges in jointly modeling OBS and MCS data is the uncertainty associated with the OBSs' locations. OBSs are deployed at the sea surface with an assumption that they will fall vertically. In presence of oceanic currents, however, this may not be necessarily true. The actual resting point of the OBS is generally unknown and location uncertainty may translate into traveltime modeling errors. We adopted a simple and intuitive method for locating individual OBSs. First, we checked for remnant clock drift by using the symmetry of the near-offset (0 – 2km) direct arrivals. Next, by merely trying to fit a NMO–type parabolic equation to the near-offset direct arrivals for all seven OBSs we obtain an average value for the ocean water velocity (1.495 km/s in this paper). This step is critical because a large part of individual raypaths are in the water column due to the seafloor depth in compare to the sediment thickness.

Following water velocity estimation, the MCS dataset is migrated with 1.495km/s with the understanding that other than the seafloor, no horizon will be correctly positioned in the migrated stack. Seafloor for the velocity–depth model to be updated from traveltime inversion is obtained in this manner. Next, using the water velocity and migrated seafloor structure, the location of individual OBSs along the seafloor is estimated in the following manner. An individual OBS is placed at a certain location at the seafloor in the velocity-depth model immediately below its deployment location, followed by simulating the seafloor reflection and comparing it to the seafloor times observed in the OBS gathers. Until the overall chi-square normalized error (χ^2 ; Bevington and Robinson, 1969) error between the predicted and observed times is less than 1ms, the process is repeatedly with a new position of the OBS. In the end, the OBS location is determined heuristically.

Reflection traveltime picking

To identify common horizons below the seafloor in MCS and OBS data, we used the strategy suggested by Jaiswal et al. (2006). In this strategy, after determining locations of the OBS along the MCS stack, a portion of the in-between MCS stack was inserted between the positive-offset half and the negative-offset half of the bounding OBSs. The OBS gathers were deepened (by half the stack seafloor time) so that the seafloor in the MCS and OBS data are aligned (Figure 3). This also served as an additional quality control step for OBSs positioning. Below the seafloor, three horizons were selected for traveltime picking – B1, B2 and B3 – based on their continuity and relevance in both GC955 and WR313 profiles. In GC955 (Figure 4a), B1 was the top of the fine-grained layer where hydrate was inferred in Well GC955-H. B2 was the first coherent and continuous reflector below the high reflectivity zone (the main hydrate reservoir) and B3 was the next deeper horizon that could be traced across the whole model. In WR313 (Figure 4b), horizons B1 and B2 are the top and base of the clay-dominant layer where fracture-filling hydrates were found. Horizon B3 marks the top of a prominent sand-dominated unit.

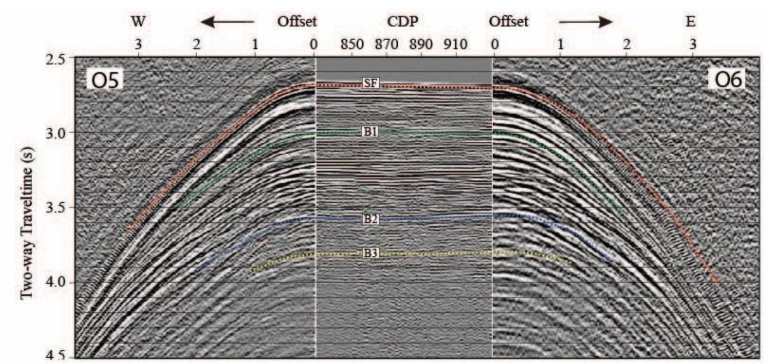

Figure 3. MCS-OBS merger. An example from GC955 profile where a section of the stack has been inserted between OBSs 5 and 6. Symbol SF indicates seafloor and horizon B1 – 3 are labeled and color coded.

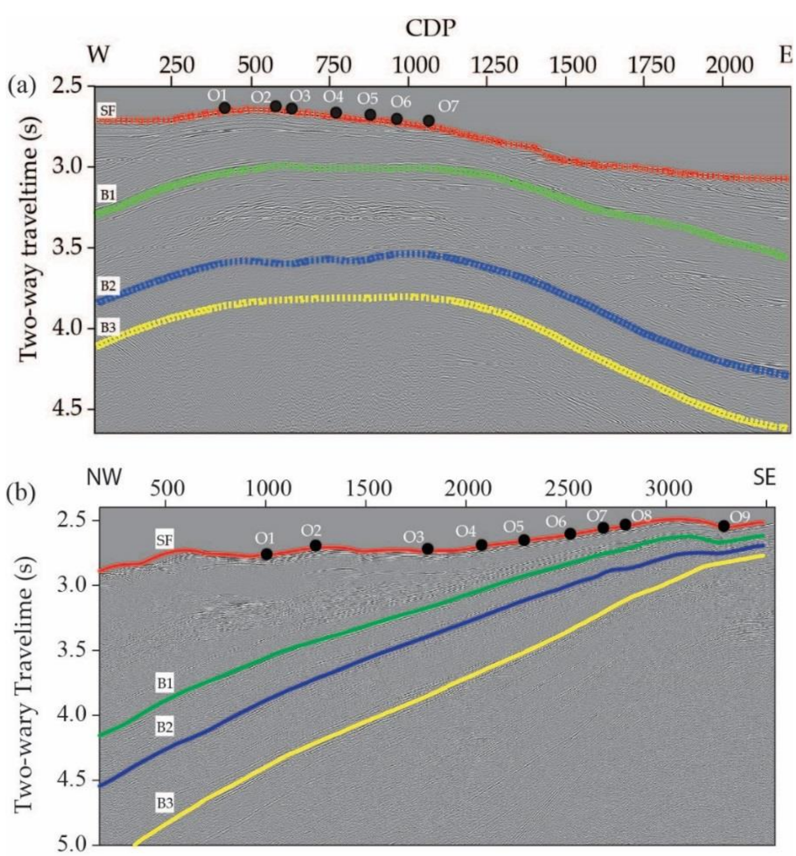

Figure 4. Stack. a) GC955 and b) WR313. In both a) and b) horizons B1 – B3 are labeled and color coded and the OBSs locations at the seafloor is also shown.

Following determination of common horizons, their arrival times were picked in both the OBS gathers and the MCS stack. OBS picking at offsets greater than 2km was challenging due to waveform mergers. In certain instances picking had to be assisted by forward modeling. Based on the noise content and dominant frequency, uncertainties of 5 ms and 2 ms were assigned to the OBS and MCS traveltime picks.

Traveltime inversion and PSDM

We have used the Zelt and Smith (1992) algorithm for traveltime inversion. This algorithm incorporates a Runge-Kutta method for ray tracing and a damped least-square method for computing model updates. The following is an overview of the algorithm, and the reader is directed to the original publication for details. In this inversion algorithm, a model is parameterized by the user in discrete layers defined by boundary and velocity nodes that are specified along each layer boundary. An irregular arrangement of trapezoids, with corners corresponding with the user-defined nodes, represents the velocity structure for the purposes of ray tracing. The velocity is linearly interpolated within each trapezoid. Rays are traced through the velocity model in an iterative search mode using zero-order asymptotic ray theory. To linearize the traveltime inversion problem, the algorithm first determines the ray paths in an initial velocity model and then updates the velocity model assuming stationary rays. The data misfit in traveltime inversion is assessed using the normalized form of a misfit parameter referred to as the chi-squared (χ2) error (Scales et al. 1990):

$$\chi^2 = \frac{1}{n}\sum_{i=1}^{n}\left(\frac{\Delta t_i}{u_i}\right)^2 \qquad (2)$$

In Equation 2, t_i is the difference between the predicted and the picked traveltime, n is the number of traveltime picks and u_i is the uncertainty associated with the i^{th} traveltime pick. A χ^2 value of unity indicates that the observed traveltimes have been fitted at their uncertainty levels and that the inverse problem has converged to an acceptable solution (the final model).

We have used Kirchoff's algorithm for PSDM. PSDM helps challenges related to non-hyperbolic reflections; the approach involves reverse-propagating seismic energy to the scatter points and thus obtaining images of subsurface reflectors defined in depth, even with limited reflection coda and rapidly varying velocity field (Bradford et al. 2006, Bruno et al. 2010, Grau and Lailly 1993, Morozov and Levander 2002, Pasasa et al. 1998). Critical to the success of PSDM is a smooth velocity model that provides a kinematically correct representation of large-scale features of the subsurface (Black et al. 1994, Gray et al. 2001, Yilmaz 2001). As such, velocity model building for PSDM is a non-trivial exercise due to the velocity sensitivity of migration in the pre-stack domain (Versteeg 1993). Conventionally, migration velocity models are based on stacking velocity analyses (SVA; (Al-Yahya 1989)), which may be imperfect, particularly when a limited range of source-receiver offsets is available. Traveltime inversion, a model-based method of estimating medium properties (V_P in this paper), could be an alternative to SVA (Lailly and Sinoquet 1996, Begat et al. 2004).

OBS processing

All OBSs, in GC955 as well as WR313, had identical operating parameters. Each OBS recorded four-component data: two horizontal particle velocities (horizontal geophones), one vertical particle velocity (vertical geophone), and one pressure (hydrophone). The sampling interval was 5 ms. Data quality was highly variable. Coupling was one of the main issues. Swell noise and reverberations were prominent in all OBS gathers but in some OBSs only a minimal amount of processing improved signal-to-noise ratio, while some others had to be abandoned due to poor data quality. The OBS data were processed in two different stages. In the first stage, they were prepared for traveltime picking. Processing for first stage was simple – a predictive deconvolution followed by 20-100 Hz bandpass filter. Processing in the second stage mainly comprised amplitude scaling (such as (Kamei and Pratt 2013)) and was meant to prepare them for FWI. Scaling is an essential step to remove effects of non-physical factors such as unequal instrument gain, source and receiver directivity, etc., that are beyond the physics of modeling. The scaling was done using the traveltime model in the following manner. A ricker wavelet was constructed with the same bandwidth as the real data and using the field geometry synthetic gathers were generated. The real gathers were scaled such that the amplitude-versus-offset (AVO) variation of their first arrival waveforms were same as the synthetic data. On a related note, amplitude scaling precluded determination of attenuation. However, a thorough before–after data comparison was made to ensure no unwanted phase rotation or amplitude artifacts have been introduced. Additionally, for FWI, the OBS data were also windowed in time and offsets; data within the dashed white box in Figure 5 was only used. The time window included data from 10 ms prior to the seafloor arrival to 10 ms after the arrival from the deepest horizon of interest. The offset window included only the near–to–mid range (0.25 – 2.75 km). As a clarification, the window sizes were not set arbitrary. There were determined to be the most optimum in a trial–and–error manner. OBSs gathers with high random noise were amplitudes could not be scaled appropriately, were not used for FWI. In GC955, out of the 10 OBSs along the profile, only 7 were used for FWI and in WR313, out of the 9 OBSs along the profile, only 6 were used for FWI.

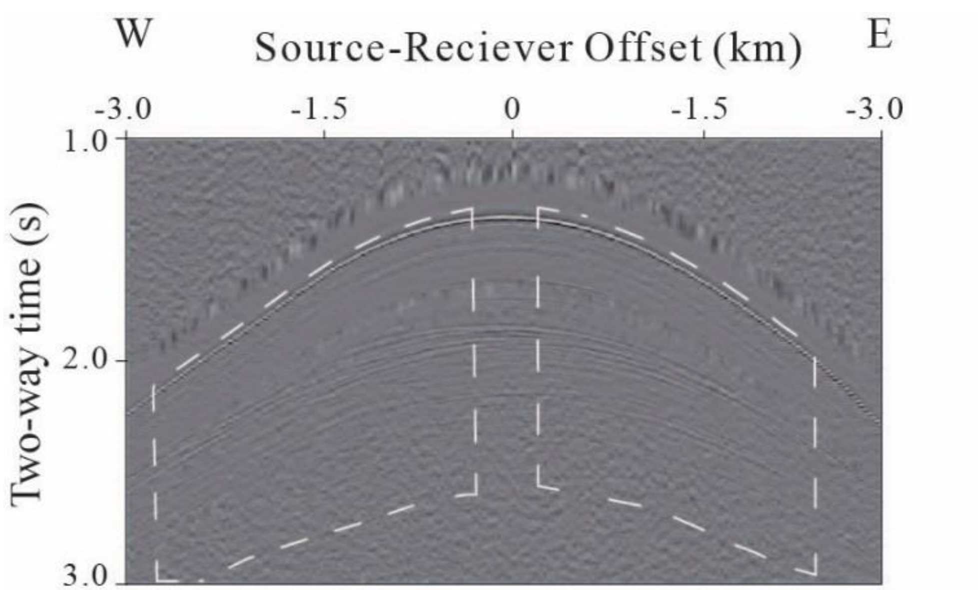

Figure 5. Part of OBS gather used for FWI. Note that the entire gather is not being used. Only the part within the dashed white line is used.

Full waveform inversion

We have use Pratt (1999) algorithm for FWI inversion. In this algorithm the elastic wavefield is modeled with an acoustic approximation. This algorithm operates in frequency domain, where the forward modeling propagates a pressure wavefield on a finite difference grid and the inverse problem iteratively updates a starting model to reduce mismatch between the predicted and observed wavefield. A brief overview of the method is provided here and the reader is guided to the original publication for details. The forward problem is solved using a mixed-grid approach (Jo et al. 1996, Štekl and Pratt 1998). Boundaries are absorbing and implemented using 45° one-way propagators (Clayton and Engquist 1977). For an individual angular frequency ω, the wave equation is expressed as:

$$d_{pre}(\omega) = S^{-1}(\omega) f(\omega) \tag{3}$$

In equation (3), d_{pre} is the complex-valued predicted wavefield vector from the model vector m, S is a complex valued impedance matrix that contains information about the physical properties of m, and f is the source term vector. The inverse problem minimizes the L2 norm of the data error, δd, expressed in an objective function, E:

$$E(m) = \frac{1}{2}\delta d^t \delta d^* \tag{4}$$

In equation (4) d is a vector comprising Fourier coefficients of the time-domain data and $d = d_{pre} - d_{obs}$, where d_{obs} is the observed wavefield, superscript t represents matrix transpose, and the superscript * represents the complex conjugate. The Taylor series expansion of $\delta E(m) / \delta m$ and its simplification in the neighborhood of m leads to the following relationship in the k^{th} iteration between the starting m^k, and the updated m^{k+1} model:

$$m_{k+1} = m_k - \alpha^k \nabla E^k(m) \tag{5}$$

In equation (5), $\nabla E(m)$ is the gradient direction and α is the step length (a scalar to replace the Hessian) that is determined by a line search method. In the (Pratt 1999) method the gradient is expressed as:

$$\nabla E(m) = \frac{\partial E}{\partial m} = \mathrm{Re}\{F^t[S^{-1}]\partial d^*\} \tag{6}$$

In equation (6), F is known as a virtual source which can be understood as the interaction of the observed wavefield d_{obs} with the perturbations in the model m. Individual elements of the virtual source are defined as $f^i = -\frac{\partial S}{\partial m_i} d_{obs}$, where f_i and m_i are the i^{th} virtual source and model parameters, respectively. Equation (5) is the mathematical expression of the back-propagated residual wavefield $[S^{-1}]\delta d$ being correlated with the forward propagated wavefield F. The computational complexity in waveform inversion mainly rests on the computation of S^{-1}. For multiple source problems, S^{-1} is best solved using LU decomposition (Press et al. 1992) and ordering schemes such as nested dissection that take advantage of the sparse nature of S (George and Liu 1981).

Rock physics modeling

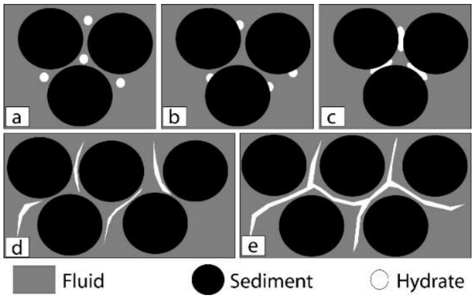

Figure 6. Cartoon of hydrate arrangement styles. (a) load-bearing; (b) suspension; (c) cement; (d) disconnected cracks; and (e) interconnected cracks. In (a) - (e) mineral grains are black; water is grey; and hydrate is white. All styles, as well as their combinations, to a certain extent, are possible at WR313 and GC955 sites.

To express the dry rock moduli as a function of porosity (ϕ), first the end member values, i.e., moduli at minimum (zero) and maximum (critical) porosity need to be computed. Between the two end members, the elastic moduli as a function of ϕ can vary in a variety of ways (Wang 2001). The two most generic classifications are based on the behavior of pore-shape changes under external pressure. When the material is unconsolidated, small change in the overburden pressure may lead to a rather large change in pore volume and, consequently, the moduli. On the other hand, for well-consolidated rocks the porosity change is linearly proportional to the change in moduli. Pores that easily deform are referred to as "soft," otherwise as "stiff." The moduli-ϕ behavior of the two pore types can be respectively described using the Lower HS bound (Dvorkin and Nur 1996) and the modified Upper HS bounds (Gal et al. 1998).

Physically, for a given ϕ, the lower and the upper HS bounds respectively present the minimum and the maximum possible moduli that can be attained in grain mixing. Jaiswal et al. (2014) extended the idea of grain mixing using HS bounds to incorporate hydrate-filled secondary porosity in background sediments (Figure 6). When the hydrate-filled secondary porosity were connected (Figure 6d), they were thought to be behaving like a stiff shell enclosing soft sediment core. Jaiswal et al. (2014) argued that by the same analogy as Gal et al. (1998), the moduli-ϕ relation of this mixture should follow the modified upper HS bounds. Likewise, the hydrate-filled unconnected secondary porosity (Figure 6e) were thought to be behaving like a stiff core enclosed by soft sediment shell. Consequently, by the same analogy as Dvorkin and Nur (1996), the ϕ-moduli relation of this mixture should follow the lower HS bound (Jaiswal et al. 2014). A summary of the floating model is presented below.

Grain mixing using the HS bounds takes the following generalized form (Mavko et al. 2009)

$$\begin{cases} K^{\min/\max} = \left[\sum_{i=1}^{n} \dfrac{fr_i}{K_i + \frac{4}{3} G_{(\min/\max)}} \right]^{-1} - \dfrac{4}{3} G_{(\min/\max)} \\ G^{\min/\max} = \left[\sum_{i=1}^{n} \dfrac{fr_i}{G_i + Z_{(\min/\max)}} \right]^{-1} - Z_{(\min/\max)} \end{cases}, \qquad (7)$$

where $Z_{(\min,\max)} = \frac{1}{6} G_{(\min/\max)} \left(\dfrac{9K_{(\min/\max)} + 8G_{(\min/\max)}}{K_{(\min/\max)} + 2G_{(\min/\max)}} \right)$.

In Equations 7, n is the number of system components. In this paper, the system components are matrix, hydrate-filled part of the secondary porosity and brine-filled part of the secondary porosity. Further, fr, K and G are the volume fraction (product of saturation and porosity), Bulk modulus, and Shear modulus of the individual system component, respectively; and subscripts 'min' and 'max' refers to minimum and maximum elastic moduli of the minerals/fluids that make up the system components. In this paper, only four minerals and fluids – quartz, clay, hydrates and brine – combined in different make up all the three system components. Thus, in Equation 6, K_{min} and G_{min} are 2.37 GPa and 0 GPa respectively corresponding to brine and K_{max} and G_{max} are 36 GPa and 45GPa respectively corresponding to quartz (Table 1). The general form of elastic velocities for the connected (C) and the unconnected (U) case is

$$V_P^{U/C} = \sqrt{\frac{K^{\min/\max} + (4/3)G^{\min/\max}}{\rho_b}}, \quad V_S^{U/C} = \sqrt{\frac{G^{\min/\max}}{\rho_b}} \tag{8}$$

where V_S is the Shear-wave velocity and ρ_b is the bulk density which is expressed as

$$\rho_b = \phi_p.\rho_p + \phi_s.\rho_s . \tag{9}$$

In Equation 9, ϕ_p and ϕ_s are primary and secondary porosities such that the total porosity, ϕ_t, is their sum total, $\phi_t = \phi_p + \phi_s$. Further, ρ_p is the density of the saturated matrix (both sediment and pore-fluid are included) and ρ_s is the density of material that fills the secondary porosity (brine and hydrate in this paper). In terms of ϕ_s, volume fractions of the three system components can be expressed as

$$fr_m = 1 - \phi_s;\ fr_s = \phi_s \cdot S_s;\ fr_b = \phi_s \cdot (1 - S_s) . \tag{10}$$

In Equation 10, fr_m, fr_s and fr_b represent saturated matrix, hydrate-filled part of the secondary porosity and brine-filled part of the secondary porosity and S_s is the hydrate saturation in the secondary porosity. The terms ρ_p and ρ_s in Equation 9 can then be expressed as

$$\begin{aligned} \rho_p &= (1 - \phi_p)\rho_1 + \phi_p \rho_2 \\ \rho_s &= f_2.\rho_h + (1 - f_2).\rho_w \end{aligned}, \tag{11}$$

where ρ_1 and ρ_2 are general expressions for solid and fluid densities in the sediment matrix and ρ_h and ρ_w are hydrate and brine density. If, in addition to being present in the secondary porosity, if hydrate is present in the matrix in pore-filling style, it will be accounted by changing ρ_1 accordingly.

In the case of unconnected secondary porosity, the system is considered as having only two components – matrix and hydrate-filled secondary porosity. The brine-filled part of the secondary porosity is incorporated into the matrix by changing the volume fractions as

$$\bar{fr}_s = \phi_s - fr_b; \quad \bar{fr}_m = fr_m + fr_b \tag{12}$$

Thus, in the case of unconnected porosity, n will be 2 in Equation 7. Although it lacks a pure physical basis, this change is needed for avoiding zero velocities which occur because of the zero shear modulus of brine.

Like ϕ_t, the total volume fraction of hydrate in the rock, fr_t, can also be expressed as a sum of individual volume fractions of hydrate in matrix, fr_p, and volume fraction of hydrate in secondary porosity as

$$\begin{aligned} & fr_t = fr_p + fr_s \\ & \Rightarrow \phi_t \cdot S_t = \phi_p \cdot S_p + \phi_s \cdot S_s \\ & \Rightarrow S_t = (\phi_m \cdot S_m + \phi_r \cdot S_r) / \phi_t \end{aligned} . \tag{13}$$

In Equation 13, S_p is the hydrate saturations in the matrix and S_t is the total hydrate saturation in a given volume of rock.

Application

GC955 Traveltime Inversion and Depth Imaging

The velocity-depth model for our profile has three layers below the seafloor that needs to be updated. We obtained the initial geometries of interfaces B1 – 3 from the water velocity depth image. Then, we carefully developed the model in a layer-stripping manner starting from the topmost layer (Seafloor – B1) and proceeding sequentially to the deeper layers. We jointly inverted the MCS and OBS reflection times but only for updating the velocities. The biggest challenge was that the ray density was not enough to simultaneously constrain the interface structure. For a given interface structure, we would try to fit the arrival times as closely as possible. Then using the updated velocity model we re-migrated the MCS data and re-interpreted the depth image to obtain the new horizon structures. In a few iterations, we were able to obtain an internally consistent velocity-depth model (Figure 7). Internal consistency implies that inverted and migrated interfaces are in close agreement (Jaiswal et al. 2008). For example, the image in Figures 7b and d are obtained from the models in Figures 7a and c and when the layer boundaries from Figure 7a and c are overlaid on Figure 7b and d, they closely mimic their migrated counterparts

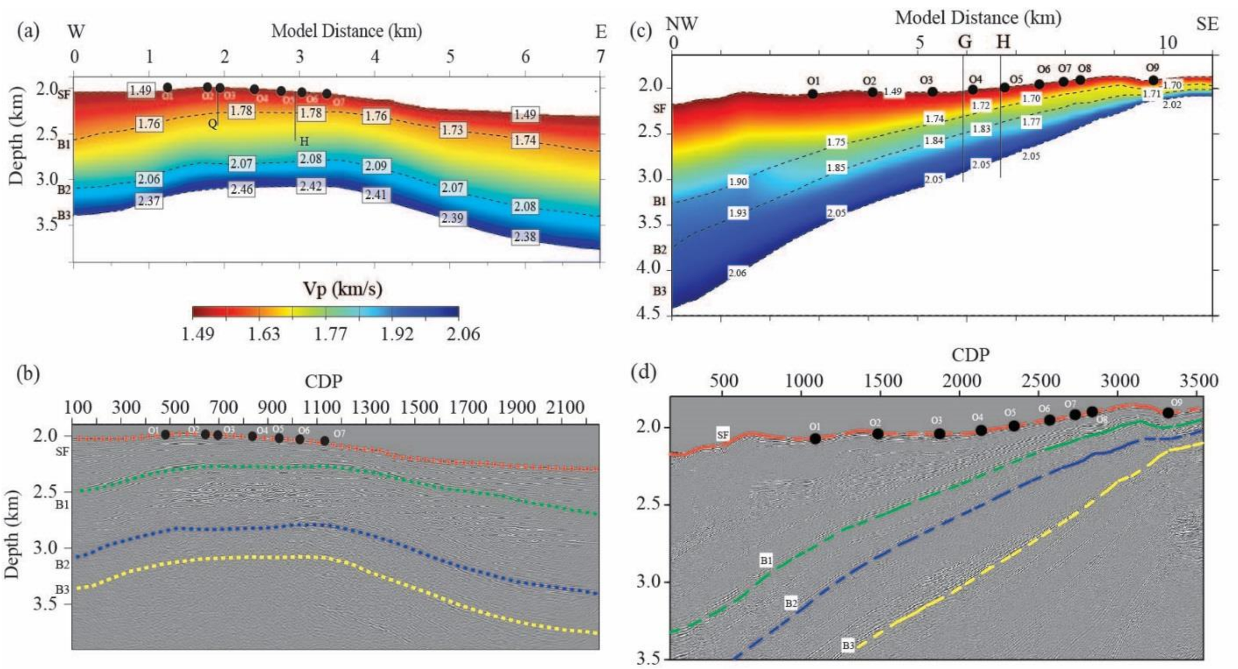

Figure 7. Models and Images. a) GC955 traveltime velocity model, b) GC955 depth migrated image, c) WR313 traveltime velocity model and d) WR313 depth migrated image. Images in (b) and (d) are migrated with models in (a) and (c) respectively. Note the correspondence in the inverted and migrated structures.

Care was taken to parameterize the traveltime model minimally. We found that velocity nodes at model distances 1km, 2.255 km (Well Q), 3.22 km (Well H), 4km, 5 km and 6.0km were sufficient not only to allow the rays to be traced to the maximum number of observation points but also to make the observed and predicted traveltimes consistent within their assigned uncertainties. The final V_P model (Figure 7a) gave an overall traveltime residual of 5 ms and a normalized $\chi 2$ of 0.819. Independently, 858 MCS traveltimes had 2 ms fit with a normalized $\chi 2$ of 0.662 and 3718 OBS traveltimes had 5 ms fit with a normalized $\chi 2$ of 0.380.

GC955 Full Waveform Inversion

We used the traveltime model (Figure 7a) as the starting model for FWI. Based on reciprocity, we modeled OBS as sources and the ship locations from where the actual shots were fired as receivers. In this manner, the source inversion required estimation of only seven “independent” waveforms (corresponding to the seven OBS gathers). The lowest usable frequency in the OBS gathers was ~8Hz. As a first step, we low-pass filtered the OBS data to make 8 – 10Hz most dominant and estimated an initial source signature by inverting 8.25, 8.5 and 8.75 Hz as a group. We used the estimated source signature for forward modeling and ensured that the simulated seafloor arrivals were within a half-cycle of the real seafloor arrivals. Then, we held the phase of the inverted source constant and updated the velocity model. This resulted in very broad and smooth model updates (Figure 7). Following this we moved to the next higher frequency bandwidth to update the source and velocity model. Instead of individual frequencies (say F) we inverted them in groups of three (F.25, F.5 and F.75 Hz) Through repeated forward modeling and data comparison, we found that not all frequency groups led to meaningful updates, maybe due to varying noise content. Following the 8Hz group, inversion of 15Hz and 21Hz groups seemed to be adequate for resolving fine-scale structure of the high-reflectivity zone (Figure 7). In every group, inversion was halted when reduction in misfit was less than 1%.

For FWI application, we found that filtering the spatial gradient was essential. The purpose of gradient filter is to limit the wavenumber content of the model and consequently mitigate spatial aliasing (Sirgue and Pratt 2004). The filter size generally depends on the minimum velocity and maximum propagation frequency but requires a through testing as horizontal and vertical filter sizes can be different (more wavenumbers are present vertically in surface seismic). The gradient filter needs to be defined for every frequency group. However, beyond the 21 Hz group, aliasing could not be prevented by gradient filtering and the model became excessively noisy. In addition to gradient filtering, we also found gradient tapering (such that the magnitude of the gradient near the seafloor decreases) to be critical. Through tapering, tradeoff in the updates between the shallower and deeper subsurface could be adjusted (Kamei et al. 2012). The model after inversion of 21 Hz frequency group was considered final (Figure 8a). Inversion of frequencies higher than 22Hz not yielding reliable results could be related to OBS spacing (~300m) (Brenders and Pratt 2007). A denser OBS spacing may have provide a tighter constrain on the model updates.

WR313 Traveltime Inversion and Depth Imaging

We picked reflection arrival times for B1 – 3 in all the 9 OBS gathers up to 4 km offsets. We were not confident in our picks beyond this offset due to waveform merger. We created the velocity-depth model in a layer-by-layer manner. First, we fixed the seafloor velocity through the OBS – MCS merging technique. Using this velocity we depth migrated the MCS stack. We used the horizon structure from the depth stack to build our velocity-depth model. We used two kinds of data for the traveltime inversion. First, are the picks from the OBS gathers. These, wide-aperture picks, constrained the velocity. We also picked B1 – 3 horizons in the stack. The stack picks acted as zero-offset reflection which prevented any unusual updates in the horizon interface. We assigned 2ms uncertainties to the stack picks. However, this was not based on the noise or frequency content but merely as weighing parameter. Our intent using the traveltime inversion was mainly to update the layer velocities, not the horizon structure. We used the updated velocity model to re-migrate the stack and generate the new depth structure. This method, originally proposed by Jaiswal and Zelt (2008), is a way of testing the consistency of a velocity model with its corresponding depth image.

After determining the seafloor structure, for inverting the B1 reflection we assigned a constant velocity gradient to the first layer (bounded by seafloor and B1) which was based on the sonic logs. Initially, we assigned a velocity node at every kilometer and also at the site locations. Then, a trial-and-error manner we added and removed velocity nodes to arrive at a minimum-parameter solution (obtain χ^2 of near unity using a minimum number of velocity nodes). Following this, we used the updated velocity model for remigration and updating the interface structure. On a related note, updating layer velocity does not change the structure of the overlying interfaces. We used the new interface structure to inverted the B1 reflections again and repeated this process until velocity updates were not significant enough to make any visible difference in migration. We continued this process for horizons B2 and B3 and developed a final velocity model (Figure 7c) and its corresponding depth migrated stack (Figure 7d). The final V_P model had an overall traveltime misfit of less than 5 ms and a normalized $\chi 2$ of 0.370. Independently, the 588 MCS (stack) traveltimes had 2 ms fit with a normalized $\chi 2$ of 0.161 and 1176 OBS traveltimes had 5 ms fit with a normalized $\chi 2$ of 0.481. Besides obtaining the data and structural fit, the geological sensibility of the final model was also used as one of the halting criteria.

WR313 Full Waveform Inversion

We used the traveltime model (Figure 7c) as starting model for FWI. Due to excessive reverberations 3 out of 9 OBS were not used for FWI. FWI was initiated with a broadband (5 – 200 Hz) minimum phase Ricker wavelet. Based on reciprocity, OBS were modeled as sources and the ship locations from where the actual shots were fired were modeled as receivers. In this manner, the source inversion only required estimation of 6 independent “sources,” one for each OBS gather. As a first step, using the traveltime model a new source was estimated. The updated source was used for forward modeling and ensure that the simulated seafloor arrivals are within half cycle of the real seafloor arrivals. Next, keeping this source fixed, the traveltime model was updated by inverting the minimum frequencies in the data - 3.25 Hz, 3.5 Hz and 3.75 Hz – simultaneously. As expected, the resulting updated were very smooth. Next, with the updated V_P model, we estimated a new source for the next group. As a clarification, every frequency group, e.g., centered around F, comprised F-0.15Hz, F Hz and F+0.25 Hz. This process was further repeated for three frequency groups centered at 4 Hz, 5.5 Hz, 8Hz and 11.75 Hz. For each frequency group, inversion was halted if the reduction in the misfit function was less than 1%.

We found that essential to obtaining a meaningful result from the FWI was the application of a gradient filter to mitigate receiver-side spatial aliasing [Sirgue and Pratt, 2004], and cosine tapering of the gradient at the seafloor to balance the updates in the deeper subsurface [Kamei et al., 2012]. The purpose of gradient filter was to limit the wavenumbers content of the model, which depends on the minimum velocity within the model and the maximum propagation frequency. The gradient filter was reset for every frequency group being inverted. We observed that beyond 11.5Hz, gradient filtering did not prevent cycle skipping and unnecessary wavenumber enhancement in the model. We considered the model from inversion of 11.25 – 11.75 Hz as final (Figure 8b).

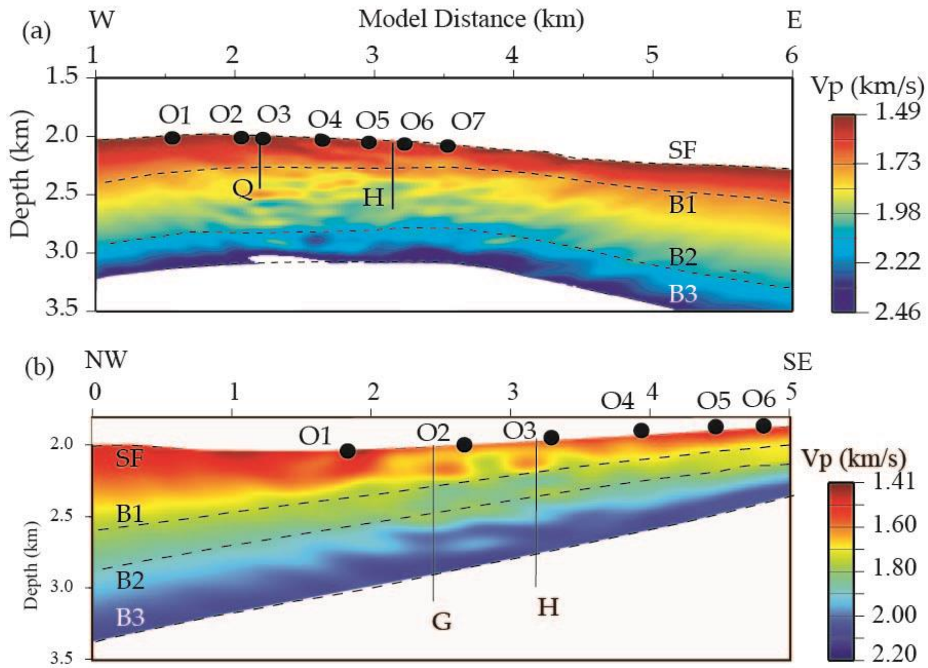

Figure 8. Final FWI models. a) GC955 and b) WR313. In (a) and (b) OBSs used in FWI have been positioned at the seafloor and labeled; wells have been labeled and their trajectories are shown; and seafloor (SF) and interfaces B1 – B3 have also been labeled.

Results

GC955 Traveltime Inversion Model

The traveltime V_P model (Figure 7a) is vertically smooth and a continuous function with no velocity jumps across the layer boundaries. Such smoothness is desirable for depth migration to avoid ringing at the layer interfaces. The comparison of the traveltime V_P model with the sonic logs at well H and Q locations (Figures 9a and b respectively) suggests that it is a fairly reliable description of the background trend.

The first velocity layer (Figure 7a) is bounded by the seafloor and B1. Both seafloor and B1 have a dome shape. The thickness of the first layer decreases from the edges (0.375 km and 0.3 km respectively at 1.0 km and 6.0 km model distances) towards the center of the model (0.2 km at model distance 4.0km; Figure 7a). Structurally, interface B1 it is highest near the Well H location (model distance ~3.25km), it has a strong reflectivity and is easily interpretable throughout the model except between OBSs O3 and O5 (Figure 7b) where it is relatively weak.

The V_P values at top of the first layer are that of the ocean water itself (1.49 km/s). At the base of the first layer, V_P increases laterally from the thicker, eastern (1.74 km/s) and western (1.76 km/s) ends towards the thinner, central part of the model (Figure 5). The V_P gradient within this layer is highest at model location 4.0 km (1.25 km/s/km). Overall, the increase in the V_P gradient (~50% from flanks to center) is proportional to the layer thickness (~50% from the flanks to crest), suggesting that V_P is dominantly compaction driven. Overall, the geometrical structure of B1 from inversion matches very well with its migrated counterpart (Figure 7a and b).

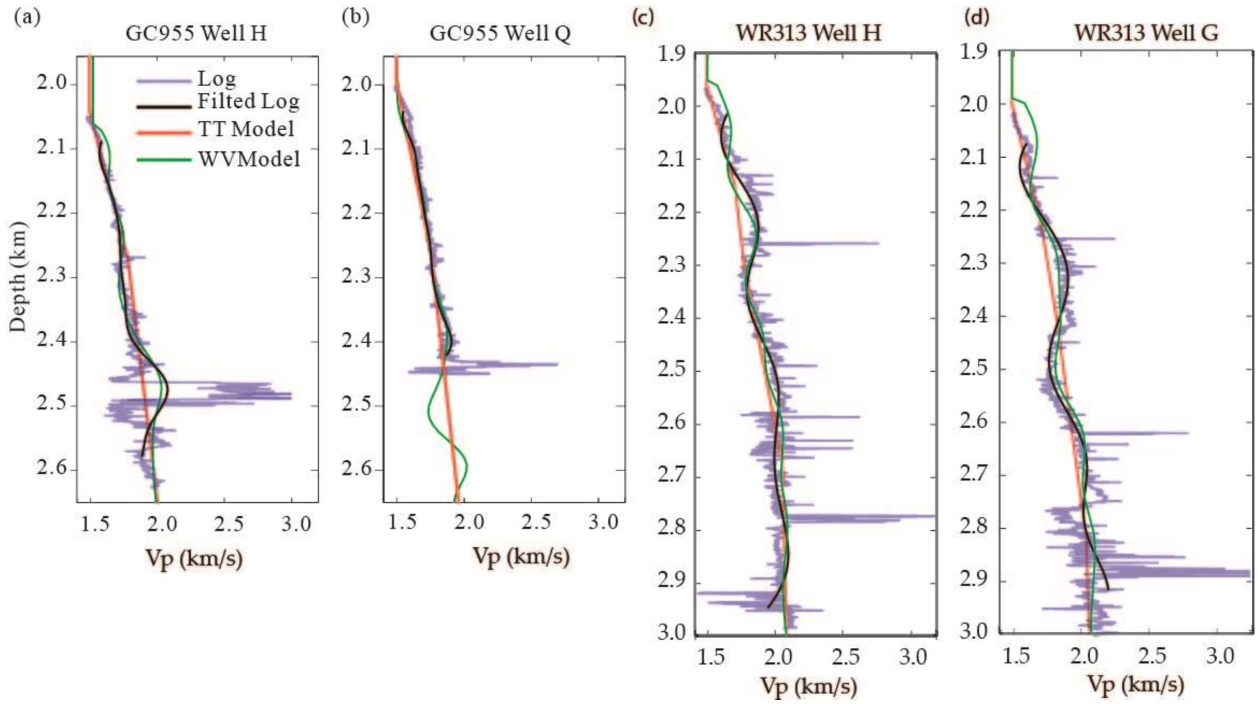

Figure 9. Log comparison. a) and b) are comparisons for GC955 and c) and d) are for WR313. Note that the traveltime velocity model provides a reasonable background trend to the sonic logs and the FWI matches the sonic log when it is low-pass filtered to contain the same wavenumbers as the FWI model.

The second velocity layer is bounded by interfaces B1 and B2. This layer contains the high reflectivity zone which was the drilling target. Much like B1, the horizon B2 can be identified as a high amplitude continuous reflector from model distances 3.5 – 7.0 km (CDPs 1200 – 2200). Within this interval, the inverted structure of B2 matches well with its migrated counterpart. From 0 km – 3.5 km model distance (CDPs 100 – 2000) its reflectivity is poor. The inverted B2 structure in this interval also has a reasonable coincidence with its migrated counterpart. At model positions west of 1.0 km the agreement between the inverted and migrated B2 structure do not match very well. This is because the second layer has the densest ray coverage between model distance 1.5 km and 4 km (CDPs 600 – 1300). As a result, the velocity model is better constrained in this zone. Consequently, the migrated structure of high reflectivity package is reliable. Our final interpretations is also limited to the zone between CDPs 300 and 1600.

Horizon B2 also has a dome shape. Structurally it is closest to the seafloor at model distance 2.4 km (~CDP 1100). The thickness of the second layer decreases laterally by ~30%, from a maximum of 0.75 km at model distance 6.0 km to a minimum of 0.54 km near Well H location. The V_P gradient is lowest at model distance 6.0 km (0.45 km/s/km) and highest at model distance 4.0 km (0.61 km/s/km). Within this layer, the V_P gradient at Well H (0.55 km/s/km) is higher than at Well Q (0.52 km/s/km). At the base of the second layer, the lowest V_P is at Well Q.

The third layer is bounded by interfaces B2 and B3, and its thickness is fairly consistent across the model. This layer is least constrained. The velocity gradient, changes by about 100%, from 0.8 km/s/km at model distance 6.0 to 1.64 km/s/km below Well Q. Relative to nearby Vp gradients (1.13 km/s/km at well H and 1.03 km/s/km at model position 1.0 km) the high gradient below well Q represents an abrupt lateral change.

GC955 Full Waveform Inversion Model

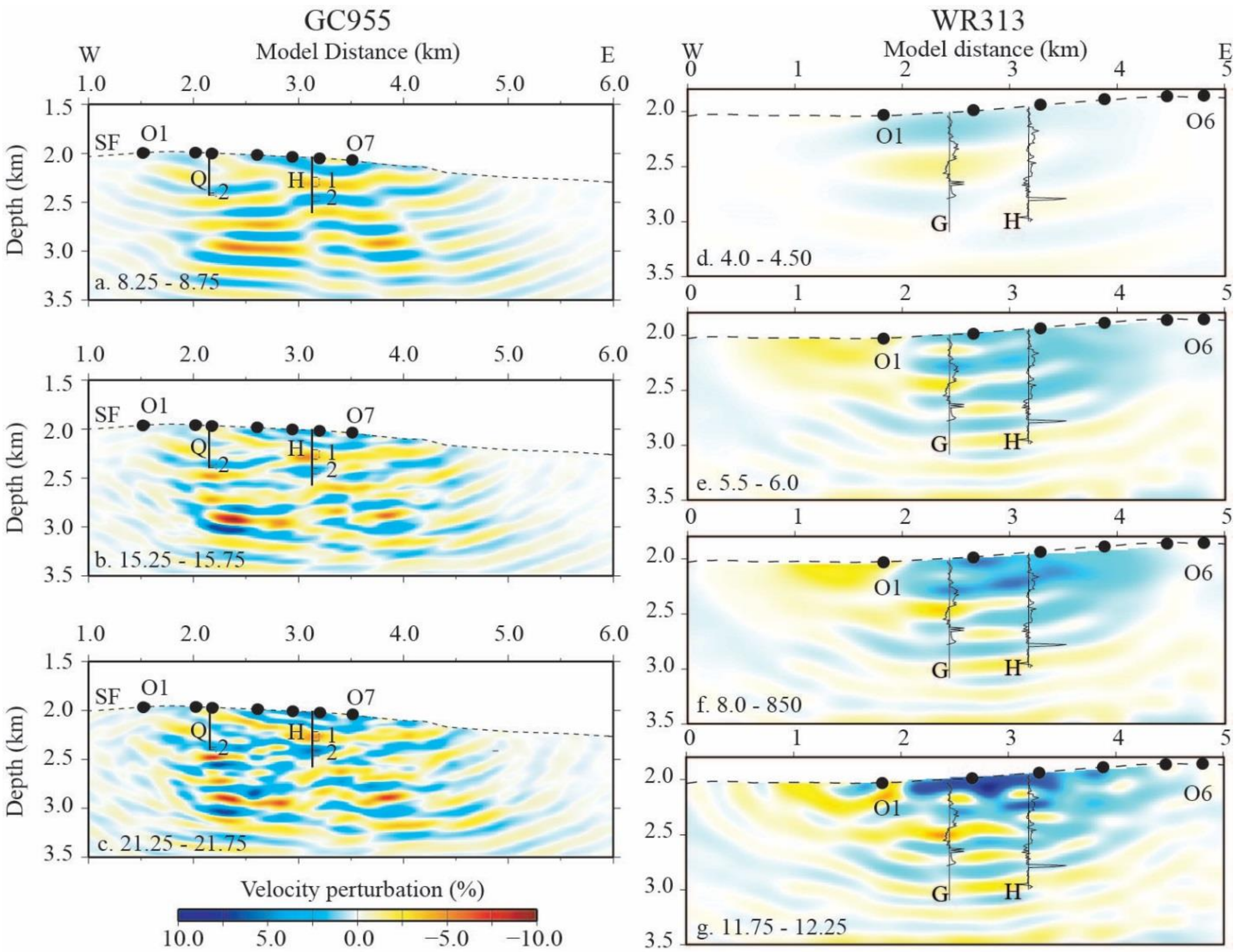

Figure 10. FWI perturbation model. (a) – (c) are models for GC955 data and (d) – (g) are models for WR313 data. In (a) – (g) the first and last OBSs have been labeled. In (a) – (c) wells have been labeled and along their trajectories indices 1 and 2 refer to the fine- and coarse-grained intervals. In (d) – (g) wells have been labeled and the sonic log has been posed along their trajectories.

Model updates from FWI were subtle, with the total change from the starting to the final model being only up to ±10%. As a result, it is more reasonable to examine the structure of the V_P perturbations, computed as $(V_P^{final}–V_P^{start})/ V_P^{start}$, for their geological sensibility than the V_P model itself. Perturbation is considered positive if V_P increases with respect to the starting model and *vice-versa*. Unlike its traveltime counterpart the fidelity of the FWI model is more difficult to assess. The FWI model needs to be interpreted with an understanding that not all perturbations may be geological. Log comparison provides a good sense of modeling reliability, at least at selected locations. In well H, the sonic log shows high velocities (>2 km/s) within ~2.45 – 2.50 km model depth (Figure 8a). The FWI V_P has positive perturbation within the same interval. At Well Q location, below the well bottom, were free gas was suspected, the FWI model shows a negative perturbation. These observations affirm that at the least the key drilling observations are being replicated by FWI.

However, care has to be taken while directly comparing the FWI model to the well logs. Logs have higher spatial resolution, i.e., a larger wavenumber range than the FWI model. To make the comparison consistent, we reconstructed the sonic logs such that they only contain wavenumbers ($0 – 10\ km^{-1}$) that were used in the vertical gradient filter of 21.25 – 21.75 Hz inversion group. The reconstructed logs are shown in black line in Figure 8. For the comparison, it appears that FWI has replicated the log velocity profile very well.

We assessed the final FWI V_P and models through quantitative and qualitative amplitude comparison. Figure 11 shows RMS error between real and simulated whole coda for 0 – 22 Hz data for both the traveltime (Figure 11a) and the FWI model (Figure 11b). For comparison in Figure 9, 0 – 22 Hz bandpass filter was applied to the real data. Figure 11 shows only a modest improvement from traveltime to the FWI model. Only modest improvements are expected from the FWI because the waveform perturbations were minor and, prior to FWI, the real data were already scaled. The fact that there is an improvement in amplitude is encouraging itself and indicative that FWI perturbations are genuine.

We also assessed the resolution of the FWI V_P by checkerboard tests. This determined the minimum dimension of the features in the V_P model that can be reliably interpreted in geological context. The starting model (Figure 7a) was perturbed in a checkerboard pattern with 10% strength and grid size of 100m and 200m. Synthetic data were generated by the finite difference code used in the full waveform inversion, and then subjected to the same inversion procedure employed to obtain the final V_P model. Results (Figure 12) suggest that in the model area beneath the OBS locations, a 100 m checkerboard pattern can be recovered to at least a depth of 500 m below the seafloor (Figure 12a), which is greater than the well depths, and the 200 m checkerboard pattern can be recovered to a depth of 800 m (Figure 12b).

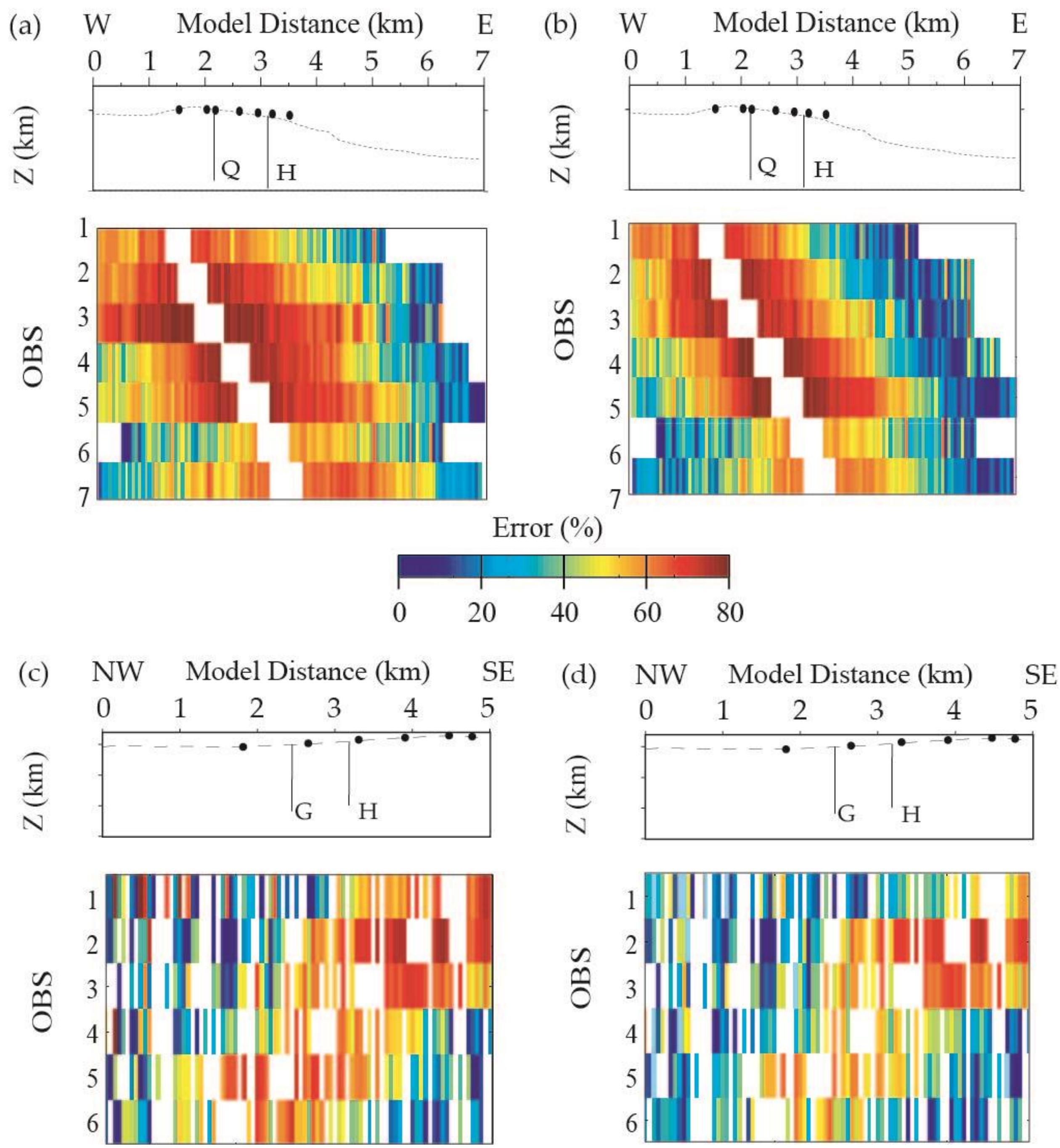

Figure 11. RMS error in predicted amplitudes from a) GC955 traveltime and b) GC955 waveform models; and c) WR313 traveltime and d) WR313 waveform models. Note the improvements from the waveform models are only modest because the waveform perturbations are fairly subtle.

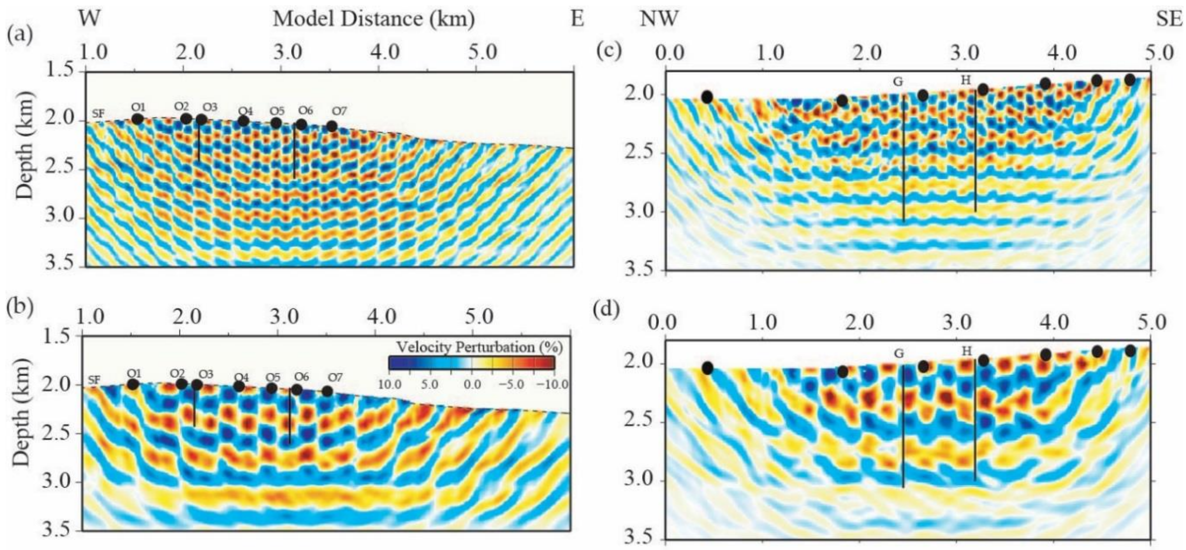

Figure 12. Checkerboard tests for a) 100m and b) 200m grid for GC955 and c) 100m and d) 200m for WR313. In (a) – (c) the wells have been labeled and their trajectories have been overlain.

WR313 Traveltime Inversion Model

The final traveltime model is constrained over a distance of ~11 km. For modeling purposes it was discretized in three layers that deepen from East to West. As a reminder, the layers boundaries were decided on the depth stack. The velocity at the seafloor is 1.49 km/s throughout the model. At the base of the first layer velocities vary from 1.70 km/s at the eastern end of the model to 1.90 km/s at the western end. The thickness of the first layer also increases from east to west and therefore the velocity gradient actually decreases from east to west. Velocities at the top of the second layer is same as at the base of the first layer, because no velocity jump across the interface was allowed in traveltime inversion. At the base of the second layer velocity increase from 1.71 km/s at east end of the model to 1.93 km/s at the west end of the model. Overall, the thickness of the second layer increases from east to west, but remains fairly constant between model distances 3.5km and 7.5 km.

The maximum vertical gradient within this layer occurs in the vicinity of sites G and H. As a reminder, this layers contained the clay unit where fracture-filling hydrate was inferred at both sites. The vertical velocity gradient increases most rapidly in the third layer. At the base of the third layer velocity increases east-to-west from 2.02 km/s to 2.06 km/s. The gradient is highest at the east end of the model and gradually decreases towards west. Overall, velocity increase with depth but is not fully conformable to the layers suggesting that the overall velocity distribution is influenced by both lithology (function of sediment type) and compaction (function of depth). A comparison between the traveltime velocities and the sonic log from sites H and G is shown in Figure 9. As expected, the traveltime velocities form a background trend of the sonic long.

Log comparison is a good way of assessing the FWI solution reliability, at least at selected locations. However, logs have higher spatial resolution (a broader wavenumber range) than FWI solution and therefore direct comparison is not justified. Instead, and to make the comparison consistent, we filtered the sonic logs such that they only contain wavenumbers up to 7 km^{-1}, which is the same as the highest vertical gradient filter set for the inversion of 11.5Hz frequency group. The reconstructed logs are shown in green line in Figure 9. From the comparison, it appears that FWI was able to replicate the sonic profile closely within 2.5 km depth at Well H and 2.7 km depth at Well G. As expected, deeper in the section, the FWI resolution deteriorates.

WR313 Full Waveform Inversion Model

Model updates from FWI were within 10% of the starting model. This is somewhat expected based on Figure 10 which suggests that the initial (traveltime) model is close to the final (sonic) model. Figure 7b shows the final FWI model from inversion of 11.5 Hz. The updates, being subtle, are not easily interpretable. It is more reasonable to examine the perturbation structure, computed as $(V_P^{final}–V_P^{start})/V_P^{start}$, for their geological sensibility than the V_P model itself. We consider a perturbation as positive if V_P increases from the starting model and *vice-versa*. A FWI model generated using the Pratt (1999) is more difficult in general to interpret than its traveltime counterpart generated using the Zelt and Smith (1992) method because unlike the traveltime inversion process, options for guiding the FWI updates are limited. The FWI model therefore needs to be interpreted with an understanding that not all perturbations may be geological (Figure 10d – g).

We also used other quantitative and qualitative methods of assessing the final FWI V_P model as well. For example, we computed the RMS error between real and simulated coda within 0 – 12 Hz bandwidth for both the traveltime (Figure 11c) and the FWI models (Figure 11d). As a clarification we applied 0 – 12 Hz bandpass filter to the real data prior to generating Figures 11c and d. The key in Figure 11 is to note the modest improvement in amplitude fit of the FWI model over the traveltime model. On a related note, due to the subtle nature of FWI perturbations and because the real data were scaled, only modest improvement in amplitude fit is expected from the FWI.

We assessed the FWI resolution by synthetic checkerboard tests, which is a common form of nonlinear assessment of tomographic solutions (Day et al., 2001; Evangelidis et al., 2004), to determine the smallest features that can be reliably interpreted in a geological context. In this test, artificially induced alternating highs and lows in a background velocity model is reconstructed in the same manner as with the real data (Lévěque et al., 1993; Rawlinson and Spakman, 2016). The starting model was perturbed with 10% strength and a checkerboard grid size of 100m and 200m. Synthetic data were generated from the perturbed model and then inverted in the same manner as the real data. The results (Figure 12) suggest that beneath the OBSs the 100 m anomalies can be recovered to at least a depth of 500 m (Figure 12c) and the 200 m anomalies can be recovered to a depth of 800 m (Figure 12d).

Discussion

GC955 PSDM image and Model

Gas hydrate accumulations at GC955 have been characterized using borehole LWD data and industry-standard 3D seismic data originally acquired and processed for deeper targets (Boswell et al. 2012b, Zhang et al. 2012, McConnell et al. 2010, McConnell et al. 2012a, Shelander et al. 2012, Hutchinson et al. 2008b). The high-resolution OBS and 2D MCS data described by Haines et al. (2014) were acquired to target the stratigraphy within the GHSZ. It employed a seismic source with high frequencies (up to 250 Hz) relative to the available industry data. Although illumination rapidly fell below the main hydrate reservoir, which is the zone of high reflectivity in the PSDM image between horizons B2 and B3 within the span of the OBSs, the 2013 USGS data served their purpose by providing a detailed view of the reservoir itself (Figure 13a).

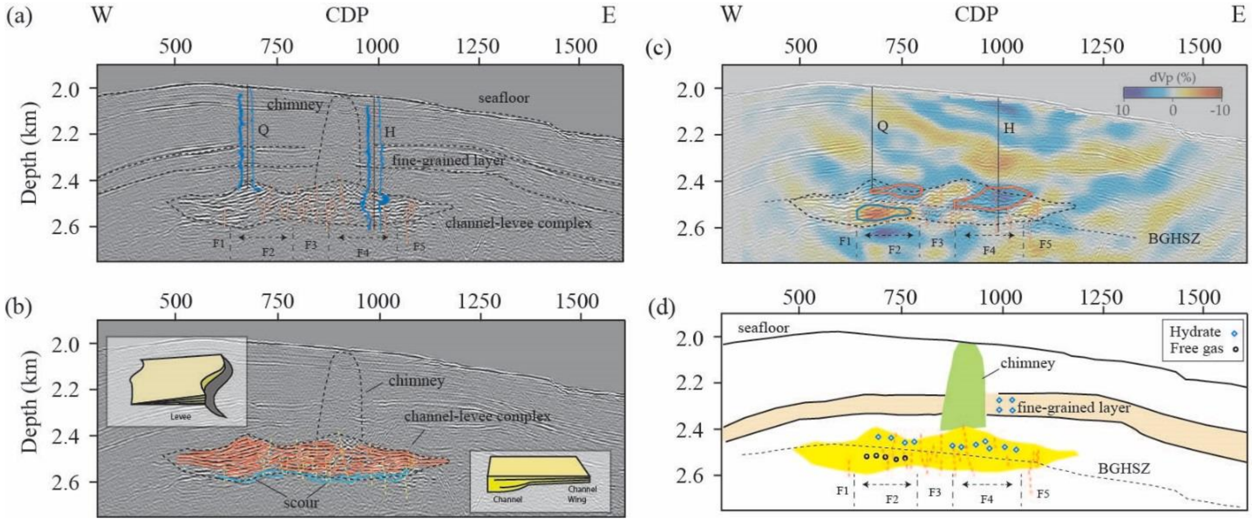

Figure 13. GC955 Joint interpretation. (a) The depth image is same as Figure 7b. Trajectories of wells H and Q are shown along with their respective gamma ray (left) and resistivity (right) logs. Outline of a chimney is interpreted with black dotted line. The fine-grained layer, where Well H found hydrate, is labeled and its top and base are interpreted. Outline of the channel-levee complex, which appears as a high reflectivity zone, is interpreted with dotted line. A chimney complex is also interpreted in dotted line and labeled. (b) Line drawings of the prominent reflectors within the channel levee complex are made with red lines. Inset shows generic geometries of a levee and channel wing (after SEPM 1990). (c) FWI perturbation model from Figure (7c) is overlaid on the migrated depth image. Well-paths for GC955-H and GC955-Q are shown and labeled. Red and blue polygons within the channel-levee complex respectively indicate +3% and -3% perturbations in turn implying hydrate- and gas-bearing sediments. (d) Cartoon showing the main architectural elements of GC955. In (a) – (d) faults are interpreted and classified into fives zone, F1 – F5. Hydrate are confined in the zones F2 and F4. Free gas is confined in the zone F2. Neither hydrate nor free gas appear to be existing within the F3 zone suggesting that both structure and stratigraphy control hydrate distribution in GC955.

In GC955 the channel-levee complex has been hypothesized as the main hydrate reservoir by Boswell et al. (2012b). We attempted to understand its internal architecture by making line drawings of the most prominent reflectors within the high reflectivity zone (Figure 13b). Although isolated sections of this high reflectivity package may bear resemblance to common fluvial features (insets; Figure 13b) such as levee and channel wings, its overall architecture is complex. We believe this is because besides amalgamated axes, overbank deposits, erosional features and such being juxtaposed against each other, the structure of the channel-levee system is also distorted by uplift due to the underneath salt movement. Further, under the influence of salt movement the channel-levee interval appears to be highly faulted, which in addition to the effects of the gas rotation and slumping, etc. complicates the direct interpretation of stratigraphy. The base of the high-reflectivity package, which we interpret as the scour feature, can be identified and appears to be fairly continuous (blue line; Figure 13b).

In absence of sonic data, it will be difficult to interpreted V_P perturbations in terms of hydrate or free gas. The Well H sonic log shows that V_P of the hydrate-bearing coarse-grained sediments is at least 30% greater than the background (Figure 8a). Through FWI, however, could only a modest, ~10%, velocity increase could be achieved. However, we have shown that within the range of frequencies considered in this paper, FWI was able to closely replicate the log. Since FWI did not exactly replicate the sonic logs, it is difficult to predict hydrate or free gas saturation along the profile. However, within the resolution obtained in this paper, the most likely hydrate- and gas-bearing zones can still be speculated.

The overlay in Figure 13c provides an interesting observation on the BHSZ. Within the GC955 channel-levee complex a BSR or any indicator of BHSZ has not been observed till date on any geophysical dataset. For estimating the base of the GHSZ, knowledge of the phase diagram of the hydrate-forming gas, seafloor temperature and geothermal gradient is needed. No geothermal gradient was measured in either Well H or Q. Based on a nearby well, McConnell et al. (2010) used of 32^0C/km gradient and 4^0C seafloor temperature for computing fluid resistivity, but these parameters could not be independently validated in the study area.

BHSZ estimated using McConnell et al. (2010) parameters and phase diagram of methane is overlaid in Figure 13c as a dashed line. It falls below the base of well Q (as expected from drilling) and clearly separates the most likely hydrate-bearing (overlying) and gas-bearing (underlying) zones. It also aligns well with the phase changes in FWI perturbation model. Phase changes in FWI merely imply that the inversion algorithm is attempting to adjust the starting model such that a better match with field data can be obtained. The fact that velocities are being adjusted across an interface which does not have any geological expression is noteworthy. We posit that this interface along with FWI phase changes are apparent (dashed line; Figure 13c) could be representing the BHSZ within the channel levee complex. A geothermal gradient of 32^0C/km is however, higher than the regional average (Jones et al. 2003).

GC955 Joint Interpretation

The channel-levee complex overlies an active salt dome (McConnell et al. 2010) in an extensional environment where faulting is expected. Faults have been known to play a significant role in hydrate systems by acting as conduits for focused fluid flow (Milkov 2000, Trehu et al. 2004, Berndt et al. 2005). The role of faults in structurally compartmentalizing the GC955 channel levee complex has been highlighted by (Zhang et al. 2012, Cook et al. 2012), however whether faults contribute to hydrate and free gas dynamics is not clear. The role of faults cannot be fully understood from a single 2D profile, but a few key observations can be made.

Based on reflection termini, we have interpreted faults, F1-F7, as prominent through-going features across the channel-levee complex on the depth image (Figure 13a). Within the resolution achieved in this paper, it appears that the most likely hydrate-bearing zone lies between F1 – F3 and F4 – F7. The most likely gas-bearing zone lies between F1 and F3 (Figure 13d). Between F3 and F4, it appears that neither hydrate nor free gas is present in any appreciable quantities (dimensions of hydrate or free gas bearing zone is below the current seismic resolution). It is possible that some faults that are compartmentalizing the channel-levee complex is also acting as barriers to lateral fluid flow. Thus, in addition to stratigraphy the hydrate and free gas could also have structural control.

A prominent feature along our profile is a chimney(Figure 13d), previously highlighted by Haines et al. (2014). The chimney, which is essentially a near-vertical zone of connected fractures, appears as region of diminished and chaotic reflectivity (Figure 13a, b). A chimney is usually considered as focused fluid flow indicator and serves as a path for gas migration (Berndt et al. 2005, Cartwright and Huuse 2005). Justification for chimneys within the GHSZ has been an open ended question mainly because it implies possibility of presence of free gas within the stability zone. Gas capillary drive has been proposed as a key mechanism for chimney formation (Cathles et al. 2010) but phase boundary roughness (Wood et al. 2002) and depletion (Liu and Flemings 2006) can also play critical role.

The FWI velocity (or perturbation) structure does not appear to be having any correspondence with the chimney and therefore we believe the chimney is a relict feature, i.e., it is not active presently. The chimney appears to be stemming from top of the channel-levee complex. However, the free gas that migrated through the chimney could have come from deeper in the section, e.g., part of the channel-levee system that is below the BHSZ. Since the channel-levee system has higher permeability, fractures from gas migration are less likely to occur.

The chimney is located close to well H and passes through a layer of fine-grained sediments where hydrate was inferred in fractures. We remind the reader that although the same layer continues westwards, no hydrate was inferred in it at the Well Q location. It is possible that hydrate in the fine-grained layer near Well H were sourced from the channel-levee complex through the chimney. For a vertical chimney to source hydrate into a shale layer, free gas will require to migrate laterally out of the chimney, which requires a certain combination of water flow, buoyancy and capillary effects (Liu and Flemings 2007). Even a thin unit at the base of the fine-grained layer with slightly elevated permeability is adequate to drive gas laterally away from the vertical chimney. Form the character of the Well H logs (Boswell et al. 2012a), permeability differences among thinly bedded units below the fine-grained layer is apparent. Within the fine grained layers, hydrate are interpreted to be occurring in vertical and near-vertical fractures (Cook and Goldberg 2008, Cook et al. 2008). This is possible though pore occlusion mechanism (Daigle and Dugan 2010) where the source of free gas is at the base of the fractured unit. Hydrate-bearing fine-grained sediment layers overlying hydrate-bearing coarse-grained sediment units have also been reported in other basins around the world, e.g. South China Sea (Zhang et al. 2015) and East Indian Margin (kumar et al. 2016). We advance an idea that chimneys are a universal phenomenon that may be linking different hydrate-bearing stratigraphy in basins worldwide.

GC955 Hydrate distribution

In seismic estimation of hydrate saturation, the rule of thumb is to establish a velocity-saturation relationship at the wellbore, say using the sonic log, and then extend it outwards using the seismic velocity field. However, for this, resolution of the seismic velocity field needs to be comparable to the sonic resolution. The FWI resolution along the GC transect is low. It does not exactly replicate the sonic log within the channel levee system. The Backus averaging is an elegant method of producing effective constants for a thinly layered medium composed of either isotropic or anisotropic elastic layers. In the case of GC955, assuming that the material is isotropic, Backus averaging of the sonic log over 30ft interval gives a fairly close match to the observed FWI log. In essence, the Backus Averaging spreads the anomalous velocity zone over a finite spatial interval. Because the porosity seems to be fairly consistent and we are assuming the mineralogy to be consistent within the channel-levee complex, it can be argued that the velocity enhancement is only due to hydrate saturation. Therefore, since we are assuming that velocity and saturation are proportional, Backus Averaging can be interpreted as spreading the hydrate over the same interval. In doing so, the total amount (or volume) of hydrate should be conserved. Thus, the saturation cannot be estimated anymore with the FWI velocity field, but possibly the volume fraction (product of saturation any porosity) could be.

Computing the volume fraction at the wellbore is fairly straightforward. Assuming a pore filling model and a mineralogy of 20% Clay and 80% Quartz (after Lee and Collette, 2012), a velocity porosity relation can be established which can be used to map the FWI velocity into saturation within the channel levee system. At the wellbore, the saturation can be converted into volume fraction using the porosity log. The challenge is extrapolating the volume fraction away from the borehole. Dutta et al. (2009) showed that both shale and clean sandstones in the Gulf of Mexico have a definitive compaction trend. We have used the Dutta et al. (2009) relation to populate porosities within the channel-levee system and using this porosity map, we are able to derive a volume fraction trend within the channel levee system (Figure 15).

Because the porosity has a smoothly varying trend, the hydrate volume fraction trend closely follows the FWI velocity map. This is by design. The relative highs and lows in the Figure 15 is an indication of the likelihood of finding hydrate. In a sense, figure 15 is a conservative estimate of hydrate saturation but an overestimate of hydrate distribution. For example, as the resolution of the velocity model increases, the saturation anomaly associated with hydrate, e.g., at Well H or in the vicinity of Well Q, will become more focused and become higher in magnitude. Thus, the hydrate in Figure 15 will get redistributed which will results in more parts of the channel-levee system with less and less hydrate.

A comparison of the current fault interpretation on the hydrate distribution suggests that the central portion of the channel-levee system has the least likelihood of having hydrate. Thus, the faults bounding the central part are probably impermeable. The eastern and the western parts, although being compartmentalized by faults, may be in communication as a whole. Boswell et al. (2012) has argued that the entire channel levee system has think layers of clay. Thus the system is likely to have a complex permeability pattern where free gas even if present below the GHSZ, may not be able to migrate into the stability zone easily and may have to stair step into it though faults. Thus, to result in such a hydrate distribution pattern, it is likely that not all faults are impermeable.

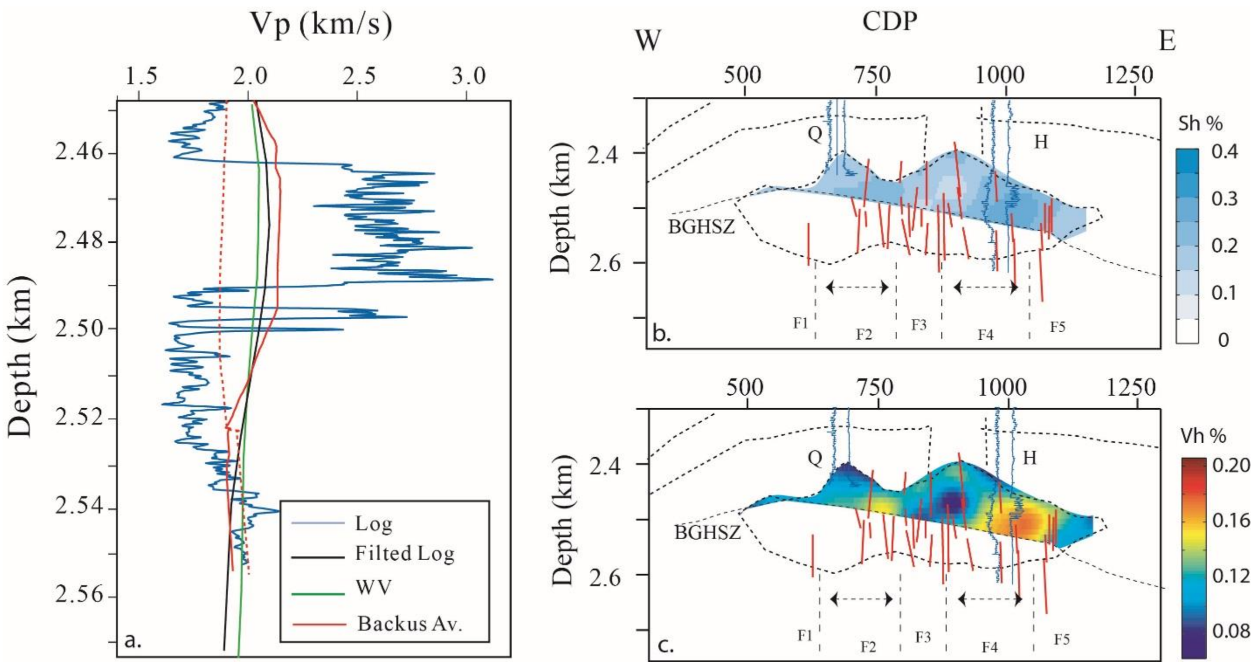

Figure 14. Saturation map. (a) Backus averaging of the sonic log. (b) hydrate saturation mapped from FWI V_P model assuming a pore filling model. (c) Hydrate volume fraction assuming Dutta et al. (20090 compaction trend. Note that faults and hydrate distribution do not appear to have correspondence indicating that the channel-levee system may be internally in communication despite being compartmentalized by faults.

WR313 Image and Model

The depth migrated image, provides an opportunity to understand structure and stratigraphy of WR313 along the currently. The layers identified as the sand-rich, “blue,” “orange” and “green” units in peer studies [McConnell et al., 2010] are appropriate color coded in Figure 15a. In addition, another unit immediately overlying the blue unit, which was suggested by Boswell et al., 2012a as containing multiple thin gas hydrate bearing layers both at Well H and G is interpreted in light blue (Figure 15a). This zone is expected to be intermediate between the coarse-grained blue unit and the fine-grained clay unit with has the fracture-filling hydrate. We will refer to it as the light blue unit. Also, much like our peer studies (McConnel et al., 2010), if we define BHSZ using a geothermal gradient of 19.5℃/km and a seafloor temperature of 3℃, a discontinuous BSR can also be interpreted (note the patchy reflectors in Figure 14a identified by red arrows). Having a discontinuous BSR along our profile in not unexpected as they have been reported frequently in the northern GoM (Shedd et al., 2010). However, in this display the patchiness itself is not very evident.

WR313 Joint Interpretation

The depth image also indicates a multitude of faulting along the profile. When carefully interpreted, there appears to be two distinct set of faults. The first set (F1 – F3; Figure 15a) dips northwest and the other (F4 – F6; Figure 15a) dips southeast. The first set lies downdip of Well G and the second set lies updip of Well H. Within the resolution achieved in this paper, Wells G and H appear to have been places in the sediments with least faulting along the profile. A majority of faults comprising the first set appear to be terminating in the fine-grained hydrate bearing layer. An overlay of the FWI velocity perturbation further suggests that zone where the first fault set terminates is also associated with a negative velocity perturbation. This is not true for the second fault set. The starting velocity values at both set of faults within the fine-grained hydrate bearing unit were fairly comparable. Thus, the velocity perturbations should not be purely driven by presence of fractures. We speculate that the first set of faults are serving as channels for fluid migration and it is possible that the fluids are originating from below the BHSZ. Further, both fault sets appear to be originating from the light blue unit. Down to the depth imaged in this paper, we do not find any overwhelming evidence of free gas (such as anomalous amplitudes, highly attenuative zones, chimney features, etc.) in our section. Only minor accumulations, creating the patchy BSZ, is suspected to be present.

The overlay in Figure 15b also provides another interesting observation – the base of BHSZ aligns well with the phase changes in the FWI perturbation model. Phase changes in FWI perturbation merely implies that the inversion algorithm is attempting to adjust the starting model such that a better match with field data can be obtained. The fact that velocities are being adjusted across an interface which does not have any geological expression is noteworthy. Thus, in this case it appears that the FWI perturbations are serving as a reasonable proxy for the BHSZ.

Based on our results we are proposing the following model for evolution of the gas hydrate system along our profile. We believe that dissolved gas is migrating updip mainly through the course gained units (e.g., blue, green, orange and light blue) from relatively distant sources (Frye et al. 2012). The first set of faults serve as additional conduits for fluids, particularly from the light blue into the clay unit. Fault F1 – F6 seems to be tectonic but within the clay unit, the fractures could be driven by hydrate formation. The second set of fault do not have a clear association with velocity anomalies, at least within the resolution achieved in this appear. We speculate that the second fault set is sealing, promoting the accumulation of hydrate within the clay unit. Why gas hydrate is restricted to a particular clay unit is not clearly understood at this stage. The mineralogy of the clay unit where fracture filling hydrate are found may be more conducive to heaving compared to the bounding unit. Or, presence of the first fault did not allow fluids to seep into any other units. Or, the gas saturation is too low to begin with to allow a widespread hydrate formation along the profile. Nonetheless, we believe that both structure and stratigraphy controls gas hydrate formation along the profile.

WR313 Hydrate Distribution

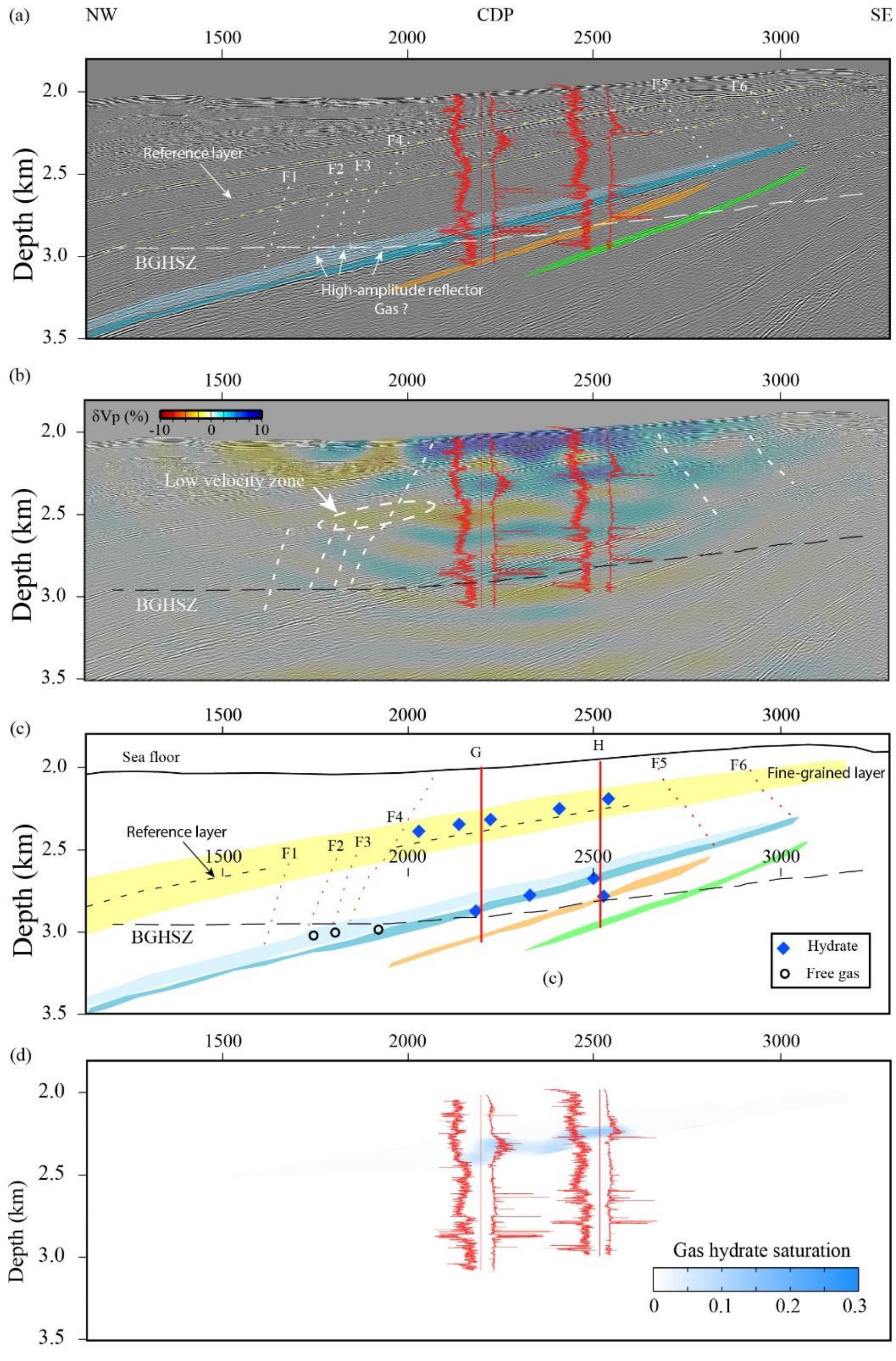

Figure 15. WR313 Joint interpretation. (a) The depth image is same as Figure 7d. Trajectories of wells H and G are shown along with their respective gamma ray (left) and resistivity (right) logs. The BSR (from peer studies) is interpreted with a white dashed line. Two sets of faults, dipping NW and SE, are also interpreted in dashed line. The fine-grained layer, where wells H and G found hydrate in fracture is labeled as reference layer and its top and base are interpreted. (b) FWI perturbation model from Figure 70g is overlaid on the migrated depth image. (c) Cartoon of the prominent stratigraphic elements along the profile. (d) Hydrae saturation based on velocities.

Model resolution achieved in this paper is too low to estimate hydrate saturation in the thinly-bedded coarse grained sediments. However, the resolution is appropriate for saturation estimate in the fine-grained unit where hydrate-filled fractures were inferred (237 - 402 mbsf in well G and 168 – 314 mbsf in Well H). Even in the fine-grained hydrate bearing unit, in absence of dipole sonic, our rock physics model will remain poorly constrained. However, we can gain first order approximation of hydrate distribution along the profile, by making some simplistic assumption and applying the Jaiswal (2015) model (presented in Section 3.3). First, we will assume that no hydrate is present in primary porosity; second, that the secondary porosity (fracture and veins) is completely saturated with gas hydrate; third, that the connected and disconnected secondary porosity are equiproportional, i.e., 50% of secondary porosity can be modeled using the lower bound and the remaining 50% using the upper bound; and fourth, that the fine-grained host material is a clay-quartz mixture.

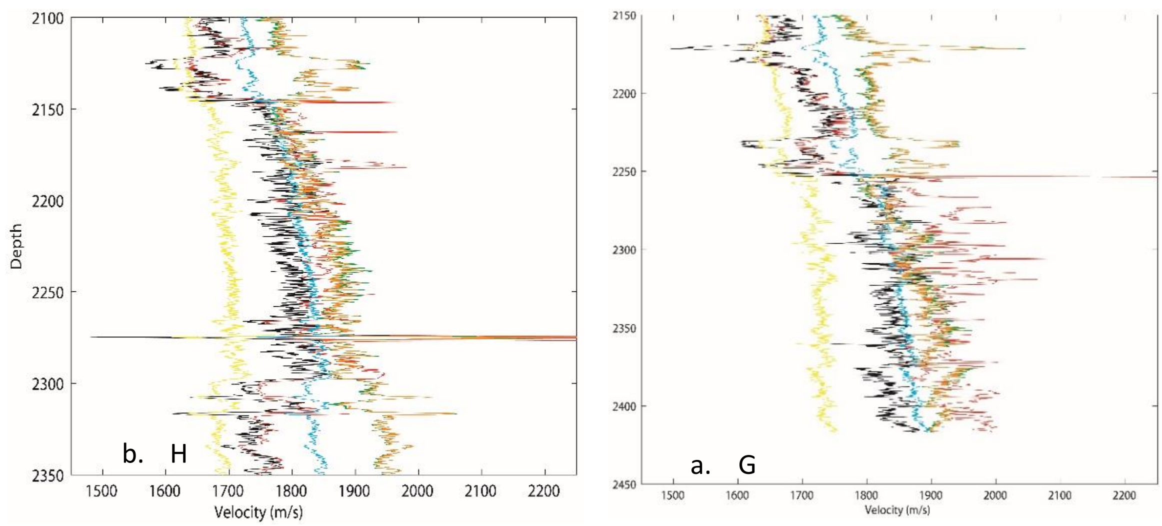

Figure 16. WR313 Saturation estimation. The sonic log is compared with different kinds of rock physics models color coded as follows. Cyan: water-filled connected secondary porosity and water-filled primary porosity; yellow: water-filled unconnected secondary porosity and water-filled primary porosity; red: log; black: water filled primary porosity and no-secondary porosity; green: hydrate-filled connected secondary porosity and water-filled primary porosity; and brown: hydrate-filled unconnected secondary porosity and water-filled primary porosity. Hydrate saturation used for the connected and unconnected porosity is shown in Figure 15d. Note that different rock physics models matches the sonic log within different depths. The interval where the secondary porosity matches the sonic log is the fine grained interval where hydrate was observed in cracks.

Log data display in Figure 12 suggests the following about the fine-grained hydrate bearing unit: a) its porosity is lower than the bounding units and internally fairly consistent, and b) c) its velocity is higher than the bounding units and fairly consistent as well. Such a velocity-porosity relation can nominally be explained even in absence of hydrate. However, to explain the anomalously high resistivity of this unit it is essential to consider presence of gas hydrate. To incorporate gas hydrate in the Jaiswal (2015) model an estimate of secondary porosity is needed. The density-porosity log with is a measure of the total porosity needs to be appropriated between primary and secondary porosity. A simple way of estimating the primary porosity is by fitting a compaction trend to the log (e.g., black curve, Figure 12a and d) similar to empirical trends proposed by Dutt et al. (2009) in the Gulf of Mexico area. Assigning a compaction-driven background trend such as the black curve in Figures 12a and d, the secondary porosity does not appear to be exceeding 5% of the total porosity. Using this porosity appropriation and using the gamma ray log (γ) as a proxy for the mineralogy (γ=80 is 90% clay and γ=50 is 60% clay), the predicted V_P for 0% S_{gh} using the Jaiswal (2015) model is shown in Figure 12c and f. The predicted V_P shows a fairly reasonable match with the sonic log at fine-grained intervals deeper in the sections at both the sites G and H where hydrate is absent, indicating that our modeling assumptions are fairly reasonable. Thus, within the fine-grained hydrate bearing unit, the difference between the 0% S_{gh} V_P and FWI V_P can be directly translated to S_{gh}. Computed S_{gh} in this manner is shown in Figure 13. From figure 13, it appears that a), S_{gh} within the fine-grained hydrate bearing unit is not uniform, it varies between 8% and 16%, and b) gas hydrate is mainly concentrated in the vicinity of wells G and H, which warrants a geological reasoning. In any case, the fracture-filling hydrate within the fine-grained unit appears to be patchy.

Conclusions

In this project, an imaging methodology for hydrate bearing sediments using sparse seismic data has been developed and demonstrated. The end product of this methodology at leased blocks GC955 and WR313 is quantitative estimates of hydrate distribution. Additionally, at both locations there is strong evidence that the base of the GHSZ, which does not appear as a clear BSR, may be manifesting in the FWI V_P perturbations. This strongly suggesting that FWI is sensitive to subtle compositional changes in shallow sediments and establishes it as a valuable tool for investigations of hydrate-bearing basins.

Using the results from this imaging methodology, following were concluded at individual sites. At GC955 the overlying fine-grained hydrate-bearing unit could have been sourced from the underlying hydrate coarse-grained channel-levee complex through a chimney feature. The channel-levee system at GC955 is compartmentalized by faults, but, of which, only a few may be impermeable. Therefore, although compartmentalized, the channel-levee system in the GC955 as a whole might be in communication except selected zones. At WR313 the overlying fine-grained fracture-filled hydrate unit appears to be sourced from below the GHSZ. The reason that only a particular fine-grained unit has hydrate, despite having lower porosity that the bounding units, could be the presence of secondary porosity (such as those formed from clay dewatering under compaction).

In conclusion, the project was a pioneering effort in in joint analysis of OBS and MCS datasets for advancing the knowledge about a hydrate and free–gas system dynamics using advanced processing methods such as FWI and depth migration. The Leg II drilling plan could have been greatly aided if the USGS seismic OBS-MCS data and this methodology be available prior to the expedition.

Component	Bulk Modulus (GPa)	Shear Modulus (GPa)	Density (g/cc)
Quartz	36.9	45	2.65
Illite	25.5	16	2.85
Hydrate	7.40	3.30	0.910
Brine	2.330	0.00	1.029

Table 1. Elastic moduli and density

References

Al-Yahya, K. 1989, Velocity analysis by iterative profile migration. Geophysics, **54**, no. 6,718-729.

Begat, S. L., H. Chauris, V. Devaux, S. Nguyen, and M. Noble. 2004, Velocity model estimation for depth imaging: Comparison of three tomography methods on a 2D real data set. Geophysical Prospecting, **52**, no. 5,427-438.

Berndt, C., J. Mienert, M. Vanneste, and S. Bünz. 2005, Gas hydrate dissociation and sea-floor collapse in the wake of the Storegga Slide, Norway. Norwegian Petroleum Society Special Publications, **12**,285-292.

Black, R. A., D. W. Steeples, and R. D. Miller. 1994, Migration of shallow seismic reflection data. Geophysics, **59**, no. 3,402-410.

Boswell, R., and T. S. Collett. 2011, Current perspectives on gas hydrate resources. Energy & Environmental Science, **4**, no. 4. doi: 10.1039/C0EE00203H

Boswell, R., M. Frye, D. Shelander, W. Shedd, D. R. McConnell, and A. Cook. 2012a, Architecture of gas-hydrate-bearing sands from Walker Ridge 313, Green Canyon 955, and Alaminos Canyon 21: Northern deepwater Gulf of Mexico. Marine and Petroleum Geology, no. 0. doi: 10.1016/j.marpetgeo.2011.08.010.

Boswell, R., M. Frye, D. Shelander, W. Shedd, D. R. McConnell, and A. Cook. 2012b, Architecture of gas-hydrate-bearing sands from Walker Ridge 313, Green canyon 955, and Alaminos canyon 21: northern deepwater Gulf of Mexico. Marine and Petroleum Geology, **34**, no. 1,134-149.

Bradford, J. H., L. M. Liberty, M. W. Lyle, W. P. Clement, and S. Hess. 2006, Imaging complex structure in shallow seismic-reflection data using prestack depth migration. Geophysics, **71**, no. 6,B175-B181.

Brenders, A., and R. Pratt. 2007, Efficient waveform tomography for lithospheric imaging: implications for realistic, two-dimensional acquisition geometries and low-frequency data. Geophysical Journal International, **168**, no. 1,152-170.

Brooks, J. M., H. B. Cox, W. R. Bryant, M. C. Kennicutt Ii, R. G. Mann, and T. J. McDonald. 1986, Association of gas hydrates and oil seepage in the Gulf of Mexico. Organic Geochemistry, **10**, no. 1–3,221-234. doi: 10.1016/0146-6380(86)90025-2.

Bruno, P. P., A. Castiello, and L. Improta. 2010, Ultrashallow seismic imaging of the causative fault of the 1980, M6. 9, southern Italy earthquake by pre ‐ stack depth migration of dense wide ‐ aperture data. Geophysical Research Letters, **37**, no. 19.

Cartwright, J., and M. Huuse. 2005, 3D seismic technology: the geological ‘Hubble’. Basin Research, **17**, no. 1,1-20.

Cathles, L., Z. Su, and D. Chen. 2010, The physics of gas chimney and pockmark formation, with implications for assessment of seafloor hazards and gas sequestration. Marine and Petroleum Geology, **27**, no. 1,82-91.

Clayton, R., and B. Engquist. 1977, Absorbing boundary conditions for acoustic and elastic wave equations. Bulletin of the seismological society of America, **67**, no. 6,1529-1540.

Collett, T., M. Riedel, J. Cochran, R. Boswell, J. Presley, P. Kumar, A. Sathe, A. Sethi, M. V. Lall, and V. Sibal. 2007, Expedition 01 Initial Reports. In Indian National Gas Hydrate Program.

Collett, T. S., M. W. Lee, M. V. Zyrianova, S. A. Mrozewski, G. Guerin, A. E. Cook, and D. S. Goldberg. 2012a, Gulf of Mexico Gas Hydrate Joint Industry Project Leg II logging-while-drilling data acquisition and analysis. Marine and Petroleum Geology, no. 0. doi: 10.1016/j.marpetgeo.2011.08.003.

Collett, T. S., M. W. Lee, M. V. Zyrianova, S. A. Mrozewski, G. Guerin, A. E. Cook, and D. S. Goldberg. 2012b, Gulf of Mexico Gas Hydrate Joint Industry Project Leg II logging-while-drilling data acquisition and analysis. Marine and Petroleum Geology, **34**, no. 1,41-61.

Cook, A. E., B. I. Anderson, J. Rasmus, K. Sun, Q. Li, T. S. Collett, and D. S. Goldberg. 2012, Electrical anisotropy of gas hydrate-bearing sand reservoirs in the Gulf of Mexico. Marine and Petroleum Geology, **34**, no. 1,72-84.

Cook, A. E., and D. Goldberg. 2008, Extent of gas hydrate filled fracture planes: Implications for in situ methanogenesis and resource potential. Geophysical Research Letters, **35**, no. 15.

Cook, A. E., D. Goldberg, and R. L. Kleinberg. 2008, Fracture-controlled gas hydrate systems in the northern Gulf of Mexico. Marine and Petroleum Geology, **25**, no. 9,932-941.

Daigle, H., and B. Dugan. 2010, Origin and evolution of fracture ‐ hosted methane hydrate deposits. Journal of Geophysical Research: Solid Earth, **115**, no. B11.

Dickens, G. R. 2001, Modeling the global carbon cycle with a gas hydrate capacitor: Significance for the latest paleocene thermal maximum. Vol. 124, Natural Gas Hydrates: Occurrence, Distribution, and Detection: AGU.

Dvorkin, J., and A. Nur. 1996, Elasticity of high-porosity sandstones: Theory for two North Sea data sets. Geophysics, **61**, no. 5,1363-1370. doi: 10.1190/1.1444059.

Frye, M. 2008, Preliminary Evaluation of In-Place Gas Hydrate Resources: Gulf of Mexico Outer Continental Shelf. Resource Evaluation Division, Minerals Management Service.

Frye, M., W. Shedd, and R. Boswell. 2012, Gas hydrate resource potential in the Terrebonne Basin, Northern Gulf of Mexico. Marine and Petroleum Geology, no. 0.

Gal, D., J. Dvorkin, and A. Nur. 1998, A physical model for porosity reduction in sandstones. GEOPHYSICS, **63**, no. 2,454-459. doi: 10.1190/1.1444346.

George, A., and J. W. Liu. 1981, Computer solution of large sparse positive definite.

Grau, G., and P. Lailly. 1993, Sequential migration-aided reflection tomography: An approach to imaging complex structures. Journal of Applied Geophysics, **30**, no. 1,75-87.

Gray, S. H., J. Etgen, J. Dellinger, and D. Whitmore. 2001, Seismic migration problems and solutions. Geophysics, **66**, no. 5,1622-1640.

Haines, S. S., P. E. Hart, C. Ruppel, T. O'Brien, W. Baldwin, J. White, E. Moore, P. Dal Ferro, and P. Lemmond. 2014, Cruise report for P1-13-LA, US Geological Survey gas hydrates research cruise, R/V Pelican April 18 to May 3, 2013, deepwater Gulf of Mexico. US Geological Survey.

Hutchinson, D. R., P. E. Hart, T. S. Collett, K. M. Edwards, D. C. Twichell, and F. Snyder. 2008a, Geologic framework of the 2005 Keathley Canyon gas hydrate research well, northern Gulf of Mexico. Marine and Petroleum Geology, **25**, no. 9,906-918. doi: 10.1016/j.marpetgeo.2008.01.012.

Hutchinson, D. R., C. Ruppel, H. Roberts, R. Carney, M. Smith, and v. in: , ed. by , ., in press May 2011. 2011, Gas hydrates in the Gulf of Mexico, in N.A. Buster and C.W. Holmes, eds., Gulf of Mexico Origin, Waters, and Biota: Texas A&M University Press.

Hutchinson, D. R., D. Shelander, J. Dai, D. McConnel, W. Shedd, M. Frye, C. Ruppel, R. Boswell, E. Jones, and T. S. Collett. 2008b, Site selection for DOE/JIP gas hydrate drilling in the northern Gulf of Mexico.

Jaiswal, P., S. Al-Bulushi, and P. Dewangan. 2014, Logging-while-drilling and wireline velocities: Site NGHP-01-10, Krishna–Godavari Basin, India. Marine and Petroleum Geology.

Jo, C., C. Shin, and J. Suh. 1996, Design of an optimal 9 point finite difference frequency-space acoustic wave equation scheme for inversion and modeling. Geophysics, **61**,329-337.

Jones, G. D., P. J. Barton, and S. C. Singh. 2003, Combined structure and velocity stacks via the tau-p transform. Geophysical Prospecting, **51**, no. 3,205-213.

Kamei, R., and R. Pratt. 2013, Inversion strategies for visco-acoustic waveform inversion. Geophysical Journal International, **194**, no. 2,859-884.

Kamei, R., R. G. Pratt, and T. Tsuji. 2012, Waveform tomography imaging of a megasplay fault system in the seismogenic Nankai subduction zone. Earth and Planetary Science Letters, **317**,343-353.

kumar, P., T. S. Collett, V. K, S. K. M, N. J, M. V. Lall, Y. Yamada, P. Schultheiss, and M. Holland. 2016, Reservoir Systems in the Offshore of India: Results of the India National Gas Hydrate Program Expedition 02. Fice in the Ice, **16**, no. 1,1-8.

Kvenvolden, K. A. 1999, Potential effects of gas hydrate on human welfare. Proceedings of the National Academy of Sciences of the United States of America, **96**, no. 7,3420-3426. doi: 10.1073/pnas.96.7.3420

Lailly, P., and D. Sinoquet. 1996, Smooth velocity models in reflection tomography for imaging complex geological structures. Geophysical Journal International, **124**, no. 2,349-362.

Lee, M., and T. Collett. 2012a, Pore-and fracture-filling Gas hydrate reservoirs in the Gulf of Mexico Gas hydrate Joint Industry Project leg II Green Canyon 955 H well. Marine and Petroleum Geology, **34**, no. 1,62-71.

Lee, M. W., and T. S. Collett. 2012b, Pore- and fracture-filling gas hydrate reservoirs in the Gulf of Mexico Gas Hydrate Joint Industry Project Leg II Green Canyon 955 H well. Marine and Petroleum Geology, no. 0. doi: 10.1016/j.marpetgeo.2011.08.002.

Liu, X., and P. B. Flemings. 2006, Passing gas through the hydrate stability zone at southern Hydrate Ridge, offshore Oregon. Earth and Planetary Science Letters, **241**, no. 1,211-226.

Liu, X., and P. B. Flemings. 2007, Dynamic multiphase flow model of hydrate formation in marine sediments. Journal of Geophysical Research: Solid Earth, **112**, no. B3.

Mavko, G., T. Mukerji, and J. Dvorkin. 2009, The Rock Physics Handbook. Second ed: Cambridge University Press.

McConnell, D., T. S. Collett, R. Boswell, M. C. Frye, W. W. Shedd, R. Dufrene, P. Godfriaux, S. Mrozewski, G. Guerin, A. Cook, and E. Jones. 2010, Gulf of Mexico Gas Hydrate Joint Industry Project Leg II: Initial Results from the Green Canyon 955 Site. Paper read at Offshore Technology Conference, at Houston, TX.

McConnell, D. R., and B. A. Kendall. 2003, Images of the base of gas hydrate stability in the deepwater Gulf of Mexico. The Leading Edge, **22**, no. 4,361-367. doi: 10.1190/1.1572091.

McConnell, D. R., Z. Zhang, and R. Boswell. 2012a, Review of progress in evaluating gas hydrate drilling hazards. Marine and Petroleum Geology, **34**, no. 1,209-223.

McConnell, D. R., Z. Zhang, and R. Boswell. 2012b, Review of progress in evaluating gas hydrate drilling hazards. Marine and Petroleum Geology, no. 0. doi: 10.1016/j.marpetgeo.2012.02.010.

McDonnell, S. L., M. D. Max, N. Z. Cherkis, and M. F. Czarnecki. 2000, Tectono-sedimentary controls on the likelihood of gas hydrate occurrence near Taiwan. Marine and Petroleum Geology, **17**, no. 8,929-936. doi: 10.1016/S0264-8172(00)00023-4.

Milkov, A. 2000, Worldwide distribution of submarine mud volcanoes and associated gas hydrates. Marine Geology, **167**, no. 1,29-42.

Milkov, A. V. 2004, Global estimates of hydrate-bound gas in marine sediments: how much is really out there? : Earth-Science Reviews, **66**, no. 3-4,183-197. doi: 10.1016/j.earscirev.2003.11.002.

Morozov, I. B., and A. Levander. 2002, Depth image focusing in traveltime map-based wide-angle migration. Geophysics, **67**, no. 6,1903-1912.

Pasasa, L., F. Wenzel, and P. Zhao. 1998, Prestack Kirchhoff depth migration of shallow seismic data. Geophysics, **63**, no. 4,1241-1247.

Paull, C. K., R. Matsumoto, P. J. Wallace, and W. P. Dillon. 1996, Proc. ODP, Init. Repts., 164. College Station, TX

Prather, B. E. 2003, Controls on reservoir distribution, architecture and stratigraphic trapping in slope settings. Marine and Petroleum Geology, **20**, no. 6–8,529-545.

Pratt, R. G. 1999, Seismic waveform inversion in the frequency domain, Part 1: Theory and verification in a physical scale model. Geophysics, **64**, no. 3,888-901.

Press, W. H., S. A. Teukolsky, W. T. Vetterling, and B. P. Flannery. 1992, Numerical Recipes (Cambridge. Cambridge Univ. Press.

Ruppel, C., R. Boswell, and E. Jones. 2008, Scientific results from Gulf of Mexico Gas Hydrates joint Industry Project Leg 1 drilling: Introduction and overview. Marine and Petroleum Geology, **25**, no. 9,819-829. doi: 10.1016/j.marpetgeo.2008.02.007.

Sassoon, D. 2010, Did Deepwater methane hydrates cause the BP Gulf explosion? The Guardian.

Scales, J. A., P. Docherty, and A. Gersztenkorn. 1990, Regularisation of nonlinear inverse problems: imaging the near-surface weathering layer. Inverse Problems, **6**, no. 1,115.

Shedd, W., R. Boswell, M. Frye, P. Godfriaux, and K. Kramer. 2012, Occurrence and nature of "bottom simulating reflectors" in the northern Gulf of Mexico. Marine and Petroleum Geology, no. 0. doi: 10.1016/j.marpetgeo.2011.08.005.

Shelander, D., J. Dai, G. Bunge, S. Singh, M. Eissa, and K. Fisher. 2012, Estimating saturation of gas hydrates using conventional 3D seismic data, Gulf of Mexico Joint Industry Project Leg II. Marine and Petroleum Geology, **34**, no. 1,96-110.

Sirgue, L., and R. G. Pratt. 2004, Efficient waveform inversion and imaging: A strategy for selecting temporal frequencies. Geophysics, **69**, no. 1,231-248.

Sloan, E. D. 1998, Clathrate hydrates of natural gases: Marcel Dekker Inc.

Štekl, I., and R. G. Pratt. 1998, Accurate viscoelastic modeling by frequency-domain finite differences using rotated operators. Geophysics, **63**, no. 5,1779-1794.

Tréhu, A. M., G. Bohrmann, F. R. Rack, and Marta E. Torres. 2003, Proc. ODP, Init. Repts., 204. Vol. 204.

Trehu, A. M., P. E. Long, M. Torres, G. Bohrmann, F. Rack, T. Collett, D. Goldberg, A. Milkov, M. Riedel, and P. Schultheiss. 2004, Three-dimensional distribution of gas hydrate beneath southern Hydrate Ridge: constraints from ODP Leg 204. Earth and Planetary Science Letters, **222**, no. 3,845-862.

Versteeg, R. J. 1993, Sensitivity of prestack depth migration to the velocity model. Geophysics, **58**, no. 6,873-882.

Wang, Z. 2001, Fundamentals of seismic rock physics. Geophysics, **66**, no. 2,398-412. doi: 10.1190/1.1444931.

Weimer, P. 1990, Sequence Stratigraphy, Facies Geometries, and Depositional History of the Mississippi Fan, Gulf of Mexico AAPG Bulletin, **74**, no. 4,425-453. doi: 10.1306/0C9B2321-1710-11D7-8645000102C1865D.

Weinberger, J. L., K. M. Brown, and P. E. Long. 2005, Painting a picture of gas hydrate distribution with thermal images. Geophys. Res. Lett., **32**, no. 4,L04609. doi: 10.1029/2004gl021437.

Wood, W., J. Gettrust, N. Chapman, G. Spence, and R. Hyndman. 2002, Decreased stability of methane hydrates in marine sediments owing to phase-boundary roughness. Nature, **420**, no. 6916,656-660.

Yilmaz, Ö. 2001, Seismic data analysis. Vol. 1: Society of exploration geophysicists Tulsa.

Zelt, C., and R. Smith. 1992, Seismic traveltime inversion for 2-D crustal velocity structure. Geophysical journal international, **108**, no. 1,16-34.

Zhang, G., J. Liang, J. a. Lu, S. Yang, M. Zhang, M. Holland, P. Schultheiss, X. Su, Z. Sha, and H. Xu. 2015, Geological features, controlling factors and potential prospects of the gas hydrate occurrence in the east part of the Pearl River Mouth Basin, South China Sea. Marine and Petroleum Geology, **67**,356-367.

Zhang, Z., D. R. McConnell, and D.-H. Han. 2012, Rock physics-based seismic trace analysis of unconsolidated sediments containing gas hydrate and free gas in Green Canyon 955, Northern Gulf of Mexico. Marine and Petroleum Geology, no. 0. doi: 10.1016/j.marpetgeo.2011.11.004.

National Energy Technology Laboratory

626 Cochrans Mill Road

P.O. Box 10940

Pittsburgh, PA 15236-0940

3610 Collins Ferry Road

P.O. Box 880

Morgantown, WV 26507-0880

13131 Dairy Ashford Road, Suite 225

Sugar Land, TX 77478

1450 Queen Avenue SW
Albany, OR 97321-2198

Arctic Energy Office

420 L Street, Suite 305

Anchorage, AK 99501

Visit the NETL website at:

www.netl.doe.gov

Customer Service Line: 1-800-553-7681